J. Fluid Mech. (1984), *vol.* 146, *pp.* 127–167
Printed in Great Britain

A unified description of two-layer flow over topography

By PETER G. BAINES
CSIRO Division of Atmospheric Research, Aspendale, Victoria, Australia 3195

(Received 15 June 1983 and in revised form 12 April 1984)

Observations of the flow of a two-layer fluid resulting from the motion of a towed streamlined two-dimensional obstacle are described in some detail. The experiments were designed to further our understanding of the factors governing the nature and magnitude of upstream disturbances in the general flow of stratified fluid over two-dimensional topography, and predictions for arbitrary two-dimensional flows are made from the results of these experiments. In particular, the relationship between uniformly stratified flow and single-layer flow over topography is suggested. Most of the observed features of interest in these experiments are nonlinear in character. Relatively complete descriptions of the observed flows are presented over a wide range of parameter values, and the phenomena observed include upstream undular and turbulent bores, bores with zero energy loss, 'rarefactions' (in which the interface height changes monotonically over a transition region of continuously increasing length), and downstream hydraulic drops and jumps. Their properties are shown to be broadly consistent with predictions from a two-layer hydrostatic model based on continuity and momentum considerations, which employs jump criteria and rarefaction equations where appropriate. Bores occur because of nonlinear steepening when the layer containing the obstacle is thinner than the other, and rarefactions occur when this layer thickness is comparable with or greater than that of the other layer. The speed and amplitude of the upstream bores are governed by nonlinear effects, but their character is determined by a balance between nonlinear steepening, wave dispersion and interfacial friction when the bore is non-turbulent.

Experimental evidence is presented for two types of hysteresis or 'multiple equilibria' – situations where two different flow states may exist for the same external steady conditions. In the first of these hysteresis types, the upstream flow may be supercritical or consist of an upstream bore state. It is analogous to the type anticipated for single-layer flow by Baines & Davies (1980) and described numerically by Pratt (1983), but it is only found experimentally for part of the expected parameter range, apparently because of interfacial stress effects. The second hysteresis type is new, and involves the presence or absence of a downstream hydraulic drop and following jump.

1. Introduction

Over the past forty years or so there has been a great deal of interest in the general nature of the flow of stratified fluids over topography. Most of these studies have been theoretical and, of these, most have utilized linearized perturbation equations and represented the topography by means of a linearized boundary condition. In many situations where the flow is two-dimensional, however, laboratory observations have

shown that an obstacle may generate motions which propagate arbitrarily far upstream, and which cause a permanent change in the velocity and density profiles upstream of the obstacle. These motions are generated over the obstacle by a nonlinear process (Baines 1977, 1979*a*). The magnitude of these upstream motions, when they occur, increases rapidly with increasing obstacle height h, and may become sufficiently large to completely block the flow at low levels. This was first demonstrated experimentally by Long (1954, 1955). In these circumstances the linear theory is of little value; in fact, it may give solutions containing unrealistic singularities for some parameter values. A recent review of relevant laboratory experiments is given in Baines & Davies (1980).

Our primary objective is to be able to calculate the flow of stratified fluid over obstacles in general circumstances. If the upstream flow incident on an obstacle is steady and may be regarded as known, the flow over and downstream of the obstacle may, in principle, be calculated numerically (leaving aside turbulence effects, separation phenomena, etc.). However, (*a*) the flow so calculated may be unstable; and (*b*) the time-dependent introduction of the obstacle into a known flow may alter the upstream flow incident on the obstacle. Hence the first requirement in the understanding of the initial-value problem for stratified flow over topography is the ability to calculate these upstream motions, i.e. one wants to be able to calculate the extra upstream flow for arbitrary (but dynamically stable) initial velocity $U(z)$ and Brunt–Väisälä frequency $N(z)$ profiles, where z is the vertical coordinate. At present, some partial answers are available for special cases, which suggest the nature of the general solution to this problem.

These special cases are as follows.

1.1. *U, N constant with height in fluid of infinite depth*

The development in time of steady-state flow over an obstacle starting from rest has been calculated by two different perturbation procedures, where the expansion has been evaluated for terms of higher order than the first. These are an expansion in powers of h (McIntyre 1972) based on small obstacle height, and an expansion in powers of N, based on the weak stratification limit, namely potential flow over a finite obstacle (Baines & Grimshaw 1979). These expansions give mutually consistent results, and both indicate that there is no influence of the obstacle sufficiently far upstream in the steady state. The solutions obtained are also very similar to those obtained by use of Long's model (e.g. Miles 1968), which yields a steady-state solution and employs the assumption that ρU^2 is independent of height far upstream. The three solutions are essentially the same when Nh/U is small, their most conspicuous feature being the downstream lee wave field. This suggests that the Long's model solution is valid over a finite range of Nh/U, namely

$$0 < \frac{Nh}{U} < \left(\frac{Nh}{U}\right)_c. \tag{1.1}$$

The value of the upper limit is unknown, but Long's model certainly breaks down when Nh/U exceeds a value at which gravitational instability (resulting in rotors and turbulence) occurs in the lee-wave field; this value depends on the obstacle shape but is of order unity.

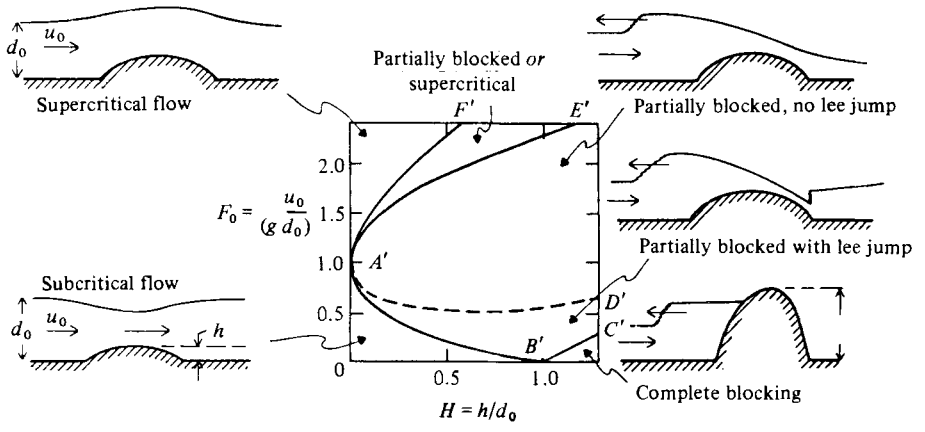

FIGURE 1. Hydrostatic single-layer flow over an obstacle. The flow regimes obtained after an impulsive start from rest for various values of F_0 and H are shown. h is the maximum obstacle height and u_0 is the speed of the obstacle relative to the initial undisturbed stream, which has depth d_0 (from Baines & Davies 1980).

1.2. *Hydrostatic single-layer flow*

Steady-state flow patterns for this system resulting from a start-up from a state of rest may be defined in terms of two dimensionless parameters

$$F_0 = \frac{u_0}{(gd_0)^{\frac{1}{2}}}, \quad H = \frac{h_{\max}}{d_0}, \tag{1.2}$$

where $h_{\max}$ is the maximum obstacle height, d_0 the initial undisturbed layer depth and u_0 the obstacle speed relative to the initial undisturbed fluid layer. In terms of these parameters, the types of flows obtained from calculations based on conservation of mass and energy in the layer are shown in figure 1. Analytical expressions exist for the solid lines and these are given in Baines & Davies (1980). The 'hydrostatic' assumption for this flow is valid for a sufficiently long obstacle; it is probably not essential for the general character shown in figure 1, but it makes the computation very much simpler. The same system of equations is also obtained for the two-layer system where the upper layer is infinitely deep and interfacial stress is negligible, which gives this example relevance for our discussion of stratified fluids. Some of the boundaries of figure 1 have been verified experimentally by Long (1970).

A glance at figure 1 shows that over most of the (F_0, H)-plane the obstacle generates substantial upstream motions which propagate to upstream infinity in an inviscid system (i.e. inviscid except for dissipation in the bore). Furthermore, the boundary of this region ($F'A'B'$ or $E'A'B'$) touches the line $H = 0$ tangentially at $F_0 = 1$, implying that nonlinear effects are significant at small obstacle heights over a broad range of Froude numbers. This upstream motion is nonlinear in both its generation and its propagation (in practice it has a bore-type structure). A linear perturbation expansion in obstacle height can describe subcritical or supercritical flow (Stoker 1953), but it breaks down as the curve $F'A'B'$ (or $E'A'B'$) is reached, and this is a very small region of validity when F_0 is near unity. This breakdown occurs because the obstacle speed approaches the long-wave speed, resulting in a resonant growth of disturbance amplitude. The region $F'A'E'$ where the flow may be either supercritical, or partially blocked with an upstream bore, has been verified numerically by Pratt (1983) and also experimentally (private communication), and it is discussed further below.

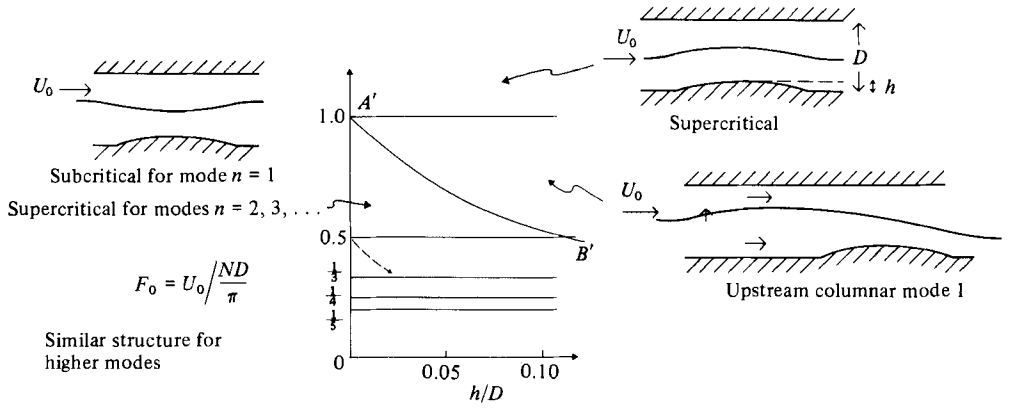

FIGURE 2. Constant-N stratified flow over a long obstacle. This figure parallels figure 1, but has been drawn from observations (figure 6(*a*) of Baines 1979*a*) with one particular obstacle. u_0 is the towing speed, N the Brunt–Väisälä frequency, h the maximum obstacle height and D the total depth. The solid line in the flow denotes a representative streamline.

1.3. *U, N constant with height in fluid of finite depth*

This system also exhibits upstream influence in some parameter ranges, but unlike the previous examples no comprehensive theory describing the observed motion yet exists. The character of the flow has been determined experimentally for some obstacles, however, and results for a fairly long obstacle are shown in figure 2 (adapted and simplified from figure 6(*a*) of Baines 1979*a*). This diagram is analogous to figure 1, and the flow is defined in terms of the dimensionless parameters

$$F_0 = \frac{u_0}{ND/\pi}, \quad \epsilon = \frac{\pi h}{D}. \tag{1.3}$$

The position of the boundary $A'B'$ depends on the obstacle shape, but the same type of behaviour is found for both long and short obstacles. Here the upstream motion is linear in character, but the generation over the obstacle is nonlinear. As for the single-layer case, linear perturbation theory can describe sub- and supercritical flow, but the solution is singular for $F_0 = 1/\text{integer}$.

1.4. *Inferences*

From the above rather limited special cases we may hypothesize that the presence or otherwise of 'upstream influence' for general (initial undisturbed) profiles $U(z)$, $N(z)$ over a finite range of obstacle height $0 < h < h_c$ depends on the following:

(i) the presence of vertically trapped long wave modes at zero (or very low) frequency and wavenumber; and

(ii) the relative motion of the obstacle should be such that one of these trapped modes is forced at or near its long-wave resonance.

The details of the response and the value of h_c will depend on the profiles $U(z)$ and $N(z)$. The reason for this behaviour may be readily understood in terms of linear-wave theory: long internal waves (wavenumber $k \to 0$) have flat dispersion curves $c(k)$, where c is the wave phase speed, so that the group velocity is equal to the phase velocity. Waves forced by an obstacle moving at this speed therefore have zero relative group velocity, and the energy may accumulate until nonlinear effects become important. These nonlinearities in the vicinity of the obstacle may then result

in upstream motions. In the first example above there is no such vertically trapped mode; in the second there is one, and in the third an infinite number.

The studies described in this paper are directed towards this general problem. They add a fourth example to the above list of cases where the upstream motion has been studied, namely two-layer flows of finite total depth, with a wide range of layer depth ratios. Laboratory studies of this system were first carried out by Long (1954), who showed examples of the various types of phenomena which can occur, and described some theoretical results for certain cases – most notably the criteria for the subcritical/partially-blocked flow boundary. Quantitative observations of the same system were made by Long (1974), where the upstream bore speed and height and the fluid depth over the obstacle were compared with theoretical predictions. In these studies the lower layer comprised 20 % of the total depth and the density ratio s was 0.9.

The only other systematic two-layer topographic experiments known to the author are those of Smith (1976), who measured lee-wave amplitudes but did not investigate upstream effects.

Houghton & Isaacson (1970) have carried out a time-dependent numerical study of hydrostatic two-layer flow over an obstacle, for the case where the two layers were of equal depth with a density ratio of 0.8, and the upper layer was bounded by a free surface. Following a larger number of numerical integrations with different initial conditions, a fairly complete description of flow types in terms of the two dimensionless parameters (a Froude number and a scaled obstacle height) was given, and some novel and interesting flow features were obtained. In particular, the upstream motion consisted of internal 'rarefactions' rather than internal bores. Interesting as these results are, it is not clear how they relate to those of the single-layer system or to systems with other layer-depth ratios. Also there are some puzzling aspects – in one flow regime unsteady flow persists just upstream of the obstacle, so that the flow does not asymptote to steady state for large times.

Keady (1971) has calculated upstream disturbances in two-layer systems, extending a method developed by Benjamin (1970), but his results are for small disturbance amplitudes and subcritical flows, and involve a number of assumptions. In particular, they assume that the lee-side disturbance is dominated by a lee-wave train, and this renders the procedure inapplicable to hydrostatic (or nearly hydrostatic) flows.

Apart from the preceding discussion, a direct motive for this study of a two-layer system was to attempt to relate the results of figures 1 and 2. One may expect that a two-layer system with a very shallow lower layer would behave in a similar manner to a single-layer system, whereas a two-layer system with layers of approximately equal depth would behave in a manner similar to that of the continuously stratified fluid of finite depth, when only the lowest mode of the latter is significant. The latter analogy is expected because the effects of wave dispersion and nonlinear steepening are similar for the two systems.

This paper is primarily concerned with two-layer systems. In a study of a continuously stratified system, McIntyre (1972) showed that some weak upstream effects may be generated in lee-wave tails under certain circumstances. These effects are not relevant to the present discussion because they have twice the vertical mode number of the generating lee waves, and hence are not present in a system with only one vertical internal mode.

In the following sections, experiments with an obstacle towed through a two-layer system consisting of kerosene and water are described, and, guided by the observations,

we develop a hydrostatic two-layer model to explain and quantify the results. Although the system has a free surface, towing speeds are low so that the external or surface mode is always subcritical, and attention is focused on the internal mode. The results are therefore applicable (with minor modifications) to any system where the internal mode is the only important one, including in particular the system with two rigid boundaries. Several phenomena are observed which have not previously been described in any detail. Emphasis has been placed on a complete description of the upstream motions. Nearly all the observed features have been explained in a qualitative sense, and good quantitative agreement has been obtained in many cases.

The plan of the paper is as follows. The experiments are described in §2, together with a general description of the various flow types observed upstream and over the obstacle. In §3 the hydrostatic theory for the motion is detailed, particularly the equations for the upstream jumps and rarefactions. In §4 the character of the upstream jumps, which take the form of undular or turbulent internal bores, is described in detail, and expressed in terms of a balance between nonlinear steepening, wave dispersion and interfacial friction. In §5 the variation of the upstream flow properties with obstacle height are discussed, together with the relation of these observations to the work of Houghton & Isaacson (1970), and the observed criteria for the existence of multiple states and hysteresis in the flow. Hydraulic drops and other downstream phenomena are described in §6, and the conclusions are summarized and discussed in §7. Possible implications for atmospheric flows are presented.

2. Experimental apparatus and observations

The experimental arrangement and procedures were similar to those of Baines (1979*a*). The experiments were carried out in a transparent tank of length 9.17 m and internal width 0.23 m. The tank was filled to a predetermined depth with fresh water (density 1.0 g cm^{-3}) and this was then surmounted by a layer of kerosene (density 0.79 g cm^{-3}). The experimental layout is shown in figure 3. A two-dimensional obstacle, which spanned the width of the tank and was supported from above the fluids, protruded downwards below the air–kerosene interface and was towed along the tank at constant speed. The resultant flow was observed by two stationary cameras, placed at points upstream, which took instantaneous pictures of the motion at regular intervals. The presence of clocks in the pictures enabled the time history of the flow to be recorded, and quantitative measurements were made from these prints. The start-up was relatively abrupt, with maximum (constant) speed being attained after a distance of less than 1 metre, and this speed was controlled with an accuracy of $\pm 1\,\%$. Two obstacle shapes were used, as given in table 1. Obstacle M1 was used for most runs; its small aspect ratio gave reasonable confidence that the local flow was approximately hydrostatic, and this is supported by comparison with the theory and the observed absence of lee waves. M2 was used where larger obstacles were required. In both cases the effective (i.e. as perceived by the fluid) obstacle height was varied by changing the depth of immersion of the obstacle; this resulted in a small degree of variation in the effective obstacle shape, which would have a negligible effect for M1. Apart from the position of the obstacle itself, the only data recorded by the cameras were the positions of the interface and free surface. From this information layer-averaged velocities were inferred.

For reasons of economy and convenience, kerosene and water were chosen as the two most suitable working fluids. The experimental arrangement described above was chosen in preference to one in which the obstacle was towed along the bottom of the

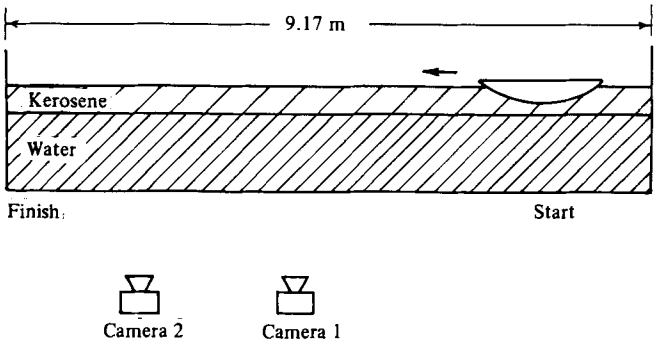

FIGURE 3. Schematic side view of experimental layout.

Obstacle number	Height h	Length $2a$	Shape
M1	2.6 cm	55.0 cm	Semi-ellipse
M2	6.0 cm	4.95 cm	'Witch of Agnesi' $z = \frac{ha^2}{x^2+a^2}$

TABLE 1

tank (as in previous studies) for the following reasons. With the obstacle on the bottom, a thin lower water layer would require a large amount of kerosene for the upper layer, which would be logistically awkward and probably make the laboratory an unpleasant place to work in for a substantial period of time. The alternative arrangement of a thin kerosene layer and a suspended obstacle is dynamically very similar provided that the motion of the air–kerosene interface is very small. This implies that the obstacle motion should be subcritical with respect to the external mode of the two-fluid system, and this limits the range of obstacle towing speeds and heights, if one aims to model the rigid lid system. In fact, as shown below (§3, figure 9), the small differences between the two systems are interesting and instructive.

In this paper we are primarily concerned with the flow upstream and over the obstacle; the flow downstream may generally be inferred if these are known, and its discussion will be postponed to §6. The various flow types observed in these experiments are shown in figure 4; numbers refer to the flow state upstream, and letters refer to the type of flow over the obstacle. The explanations of, and justifications for, the terminology are given in the succeeding sections. Type 1A denotes flow which is everywhere subcritical, and type 2B denotes flow which is everywhere supercritical. We define these terms to mean that the local Froude number (the obstacle towing speed u_0 divided by the *local* linear interfacial long-wave speed) is either less-than or greater-than unity. In the subcritical case the flow upstream of the obstacle is not affected by the latter part from transients, as for single-layer flow; on the downstream side, again only transient disturbances are present if the flow is hydrostatic (i.e. the obstacle is sufficiently long and smooth) – if the flow is not hydrostatic, lee waves may occur in the subcritical case.

For the situations where permanent upstream effects are present in the steady state, three types of upstream motion (numbered 3, 4 and 5) were observed. Type 3

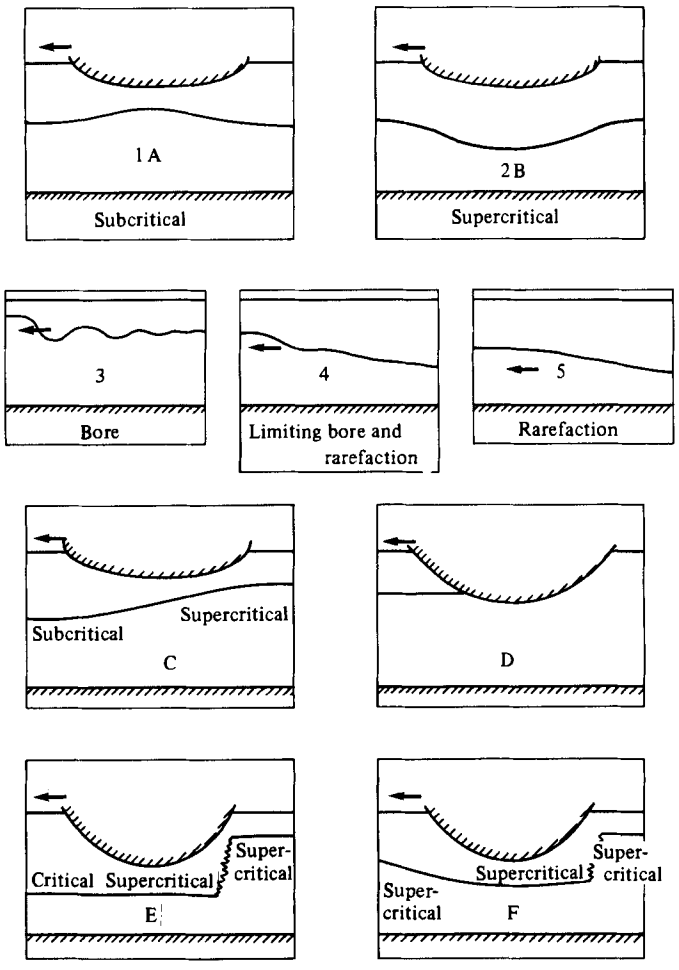

FIGURE 4. The various flow types observed in these experiments. Numbers refer to the type of flow upstream and letters refer to flow type over the obstacle. In the upstream types a distinction is made between sub- and supercritical flow.

denotes an internal bore, which was generally undular in character, although at large amplitudes the undulations were partly turbulent. Type 4 denotes a 'limiting' bore without undulations or energy loss, followed by a gradual increase in the upper-layer depth which is interpreted as a 'rarefaction', and type 5 is a pure rarefaction. If the layer containing the obstacle is the thinner of the two, then when the obstacle height is increased the upstream disturbance initially has the form of an undular bore; as the obstacle height is increased further the bore amplitude increases until the point is reached where its energy loss falls to zero and the bore takes on a limiting monotonic form without undulations. This bore travels at the maximum speed of any (internal) upstream disturbance. If the obstacle height is increased further so that the upstream disturbance is also increased, this added disturbance travels at a speed which is slower than the limiting bore; further increases in amplitude travel progressively slower still, so that this part of the upstream disturbance is continually extended with time and is termed a 'rarefaction'. The terminology is borrowed from the analogous situation in gasdynamics. Whether

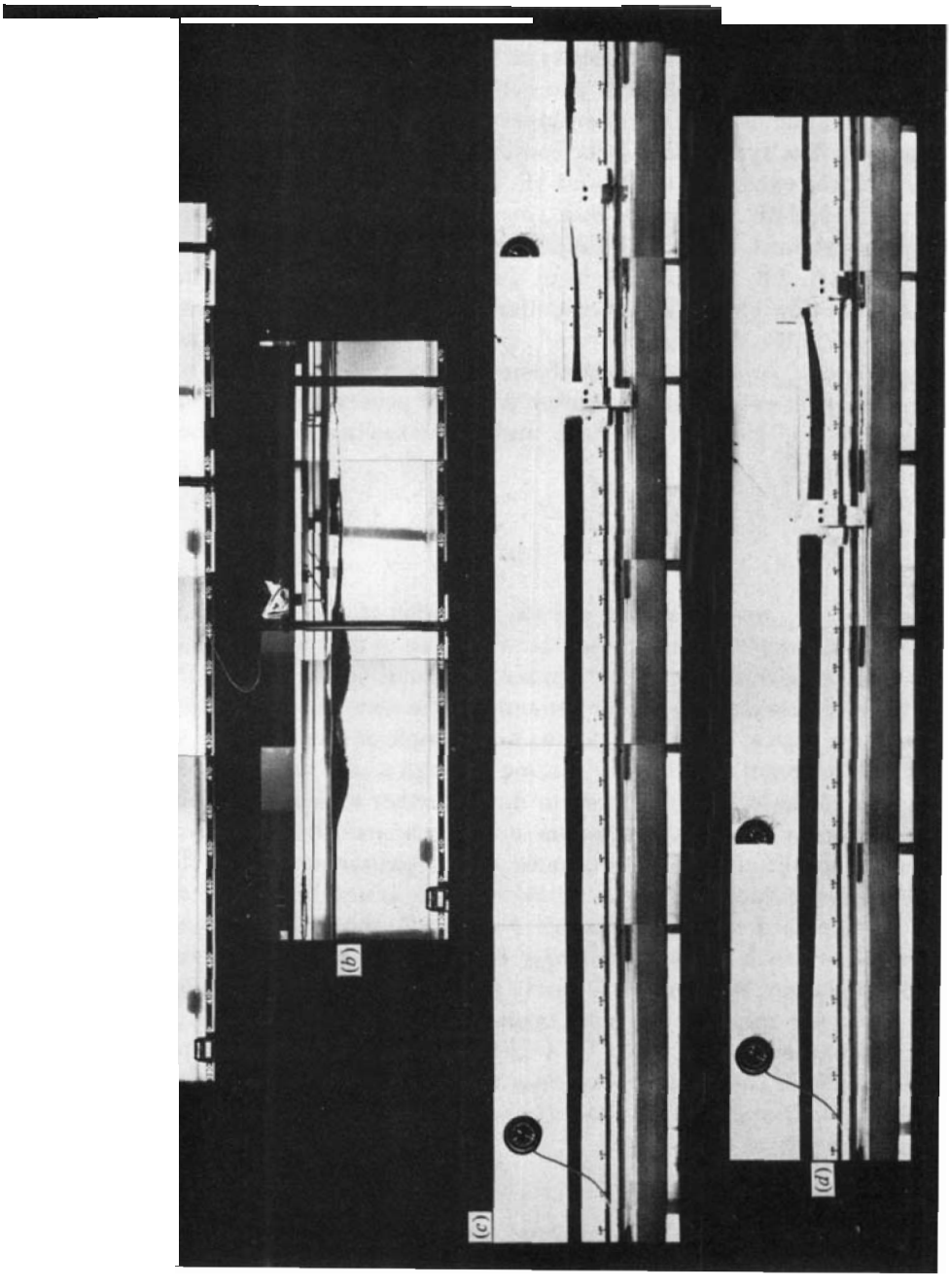

FIGURE 5. Examples of observed flows. (*a*) Upstream undular bore. Type 3C, $r = 0.0345$. (*b*) Same as for (*a*) but with larger obstacle speed. The bore is now partly turbulent. Type 3C, $r = 0.035$. (*c*) Upstream limiting bore ($dE_T/dt = 0$) and rarefaction. Type 4C, $r = 0.35$. (*d*) As for (*c*) but with larger obstacle speed. The flow over the obstacle now contains a laminar hydraulic drop on the downstream side. Type 4E, $r = 0.35$.

undular or partially turbulent, the bores propagate without changing shape, whereas the rarefactions become increasingly extended and flattened as time progresses.

With these upstream flow types there are also three associated types of motion over the obstacle, denoted C, D and E. For type C the flow is critical at the obstacle crest, passing from sub- to supercritical; for type D the upper layer is totally blocked, and for type E the flow is supercritical and symmetric at the obstacle crest and passes through a hydraulic drop to another supercritical state on the lee side. Any of the three upstream flow types 3–5 may be combined with any of the three states over the obstacle, with the exception of 3E and 3F. In addition, there is also the state which we may term type 2F, where the flow is supercritical upstream so that there is no upstream disturbance, but a hydraulic drop occurs on the lee side.

Flow types 1A, 2B, 3C and 3D occur with single-layer flows. We now give some examples of the flow types that are peculiar to the two-layer case. The most suitable way of specifying the flow parameters is in terms of the values at the initial state. We define D and d_{10} (d one–zero) to be the undisturbed total depth and upper kerosene layer depth respectively, h the maximum depth of penetration of the obstacle below the undisturbed air–kerosene interface, and u_0 the towing speed of the obstacle. We then define

$$r = \frac{d_{10}}{D}, \quad F_{10} = \frac{u_0}{\left(g\frac{\Delta\rho}{\rho_1}d_{10}\right)^{\frac{1}{2}}}, \quad s = \frac{\rho_1}{\rho_2}, \tag{2.1}$$

where $\Delta\rho = \rho_2 - \rho_1$, and ρ_1 and ρ_2 are the densities of the upper and lower layers respectively.† Long (1954) has presented examples of flow types 1 and 2 and states C, D and E over the obstacle, for two immiscible fluids with $s = 0.975$ (here $s = 0.79$). Here we show some examples for the present system which demonstrate the character of the upstream states. Figure 5(*a*) shows an example of flow type 3C, with a laminar undular bore upstream and the flow passing through a critical state over the obstacle. As time evolves the bore is observed to move further ahead of the obstacle as new wave crests appear at the latter. As one moves rearward from the head of the bore and the wave amplitude decreases because of dissipation (see §4), so that eventually the interface immediately upstream of the obstacle is nearly horizontal, with steady flow and an increased upper-layer depth. Figure 5(*b*) shows another example of type 3C where the obstacle velocity is larger than in 5(*a*) so that the bore speed and amplitude are larger, resulting in a partly turbulent internal bore. Figures 5(*c*) and (*d*) show a deeper upper layer with types 4A and 4C respectively; both have a 'limiting' bore upstream followed by a rarefaction. In 5(*c*) the flow passes through a critical state over the obstacle, whereas with the higher speed in 5(*d*) the critical state is not possible and the flow passes instead through a (mostly) laminar hydraulic drop on the lee side of the obstacle.

3. Hydrostatic theory

Guided by the observations described above, we develop a model for the fluid motion which is based on the assumption that the flow is predominantly hydrostatic, except for various postulated phenomena such as hydraulic jumps (or bores), drops,

† The proper Froude number is normally $F_0 = u_0/c$, where c is the upstream wave speed; however, the present system has a free surface upstream but a rigid upper surface under the obstacle. This difference introduces complications which are discussed in §3. Here we compromise and choose F_{10} because of its simplicity.

and rarefactions. Simple consideration of the equations of motion shows that, apart from 'discontinuous' phenomena such as jumps and drops, the flow will be hydrostatic if the forcing (in this case the obstacle) is sufficiently long and smooth so that horizontal scales are much greater than vertical scales. Although most features of the model are not new, the presentation given here is more unified and complete than previous versions, and incorporates the details of the particular system used in the experiments.

Equations for the two-dimensional flow of n layers where the ith layer has density ρ_i, horizontal velocity u_i and thickness d_i, may be written

$$\left.\begin{aligned} \frac{\partial d_i}{\partial t}+\frac{\partial}{\partial x}(u_i d_i) &= 0, && (3.1a)\\ \frac{\partial u_i}{\partial t}+u_i\frac{\partial u_i}{\partial x} &= -\frac{1}{\rho_i}\frac{\partial \overline{p}}{\partial x} && (3.1b)\end{aligned}\right\} \quad (i=1,\ldots,n),$$

where the overbar denotes a vertical average in the layer, u_i is independent of z in each layer, p denotes pressure and z is the elevation above the tank floor. At any given point within the ith layer in a hydrostatic flow we have

$$p(x,z,t) = p_s+g\sum_{j=1}^{i-1}\rho_j d_j+g\rho_i\left(\sum_{j=i}^{n+1} d_j-z\right), \tag{3.2}$$

where p_s denotes the pressure above the topmost layer; the layers are numbered downward, and $d_{n+1}(x)$ denotes a possible lower obstacle ($d_{n+1}=0$ for a flat surface). For two layers with a horizontal lower surface the equations of motion become

$$\left.\begin{aligned} \frac{\partial u_1}{\partial t}+\frac{\partial}{\partial x}\left(\tfrac{1}{2}u_1^2+g(d_1+d_2)+\frac{p_s}{\rho_1}\right) &= 0,\\ \frac{\partial u_2}{\partial t}+\frac{\partial}{\partial x}\left(\tfrac{1}{2}u_2^2+g\left(\frac{\rho_1}{\rho_2}d_1+d_2\right)+\frac{p_s}{\rho_2}\right) &= 0.\end{aligned}\right\} \tag{3.3}$$

If the uppermost layer has a free upper surface we may take

$$p_s = 0. \tag{3.4}$$

If instead it has a rigid surface we have

$$d_1+d_2 = D-h(x), \tag{3.5}$$

where D is the initial undisturbed total depth and h is the penetration of the obstacle below this depth. Here p_s may be eliminated from (3.3) by subtraction, so that in each case we have four equations for the variables u_1, d_1, u_2 and d_2.

The above equations may be integrated numerically, and this has been done for some cases by Houghton & Isaacson (1970). The process is complicated by the fact that discontinuities in the form of hydraulic jumps develop in the flow, and jump conditions must be invoked in order to continue the solutions beyond the times at which these occur. Here we adopt instead the simpler procedure of looking for 'steady' solutions which have the jump structure suggested by the experiments, following Houghton & Isaacson and Long (1970, 1974).

Flow types 1A and 2B involve no jumps and are relatively simple. The notation for type 3C is shown in figure 6, and this flow involves an upstream 'jump'. In these experiments these jumps take the form of turbulent or undular laminar bores, and they are discussed in detail in §4. In every observed case for both types of bore, variations in interface height decreased downstream from the bore front, so that (after

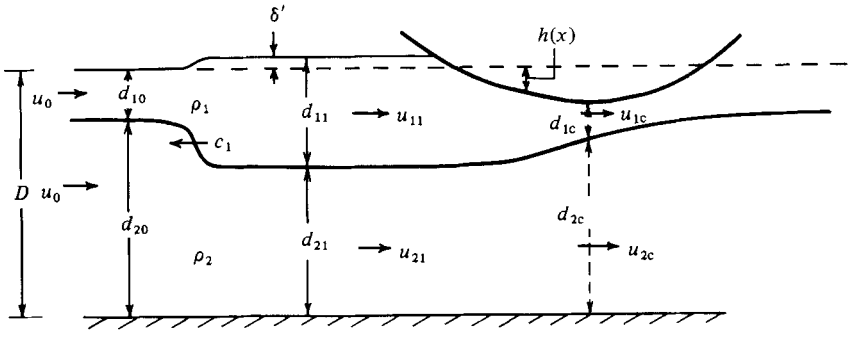

FIGURE 6. Notation for flow types 3C, with axes fixed relative to the obstacle. c_1 denotes bore speed directed upstream.

sufficient time) the bore resulted in a change from one horizontal flow state to another. For present purposes, a study of the detailed mechanics of such jumps may be circumvented by making simple assumptions about their dynamics, in order to obtain a relationship between the jump speed and its amplitude. The principal assumption is that the bore propagates along without changing shape. One equation relating conditions across the jump may be obtained from conservation of total momentum expressed as the flow force, i.e.

$$\int_0^{D+\delta'} (p+\rho u^2)\,\mathrm{d}z = \text{constant}, \tag{3.6}$$

in the frame of reference moving with the jump, where $\delta'(x)$ is the displacement of the upper free surface from its upstream position. This equation is valid regardless of the nature of the jump, provided that viscous stresses on the tank floor are negligible. Applying (3.6) across the jump and using the notation defined by figure 6, we obtain

$$\begin{aligned}\frac{(u_0+c_1)^2}{g}\left\{\rho_2\frac{d_{20}(d_{11}-d_{10}-\delta')}{d_{20}-(d_{11}-d_{10}-\delta')}-\rho_1\frac{d_{10}(d_{11}-d_{10})}{d_{11}}\right\}&\\ =(d_{11}-d_{10})\{(\rho_2-\rho_1)d_{20}-\tfrac{1}{2}(\rho_2-\rho_1)(d_{11}-d_{10})+\rho_2\delta'\}&\\ -\delta'\{\rho_1 d_{11}+\rho_2 d_{20}+\tfrac{1}{2}\rho_2\delta'\},&\end{aligned} \tag{3.7}$$

where u_0 and c_1 are both positive. This is an equation relating c_1, d_{11} and δ', and will apply for all jumps regardless of processes at the interface. To obtain speed c_1 as a function of jump height d_{11} we need an additional equation. If we assume (i) tangential interfacial stresses (turbulent and viscous) in the jump are negligible and (ii) flow in the jump is hydrostatic, and consider the momentum equation for the upper layer alone, we may obtain from (3.1) and (3.2) (e.g. Su 1976)

$$d_{11}(u_{11}+c_1)^2-d_{10}(u_0+c_1)^2+\tfrac{1}{2}g(d_{11}^2-d_{10}^2)=-g\int_{\text{upstream}}^{\text{downstream}} d_1\frac{\partial d_2}{\partial x}\,\mathrm{d}x. \tag{3.8}$$

For the flows studied in this paper the free-surface displacement δ' will be small compared with the interfacial displacement and, if we also assume that (iii) δ' is proportional to the interfacial displacement $d_{11}-d_{10}$, it follows that

$$\int_{\text{upstream}}^{\text{downstream}} d_1\frac{\partial d_2}{\partial x}\,\mathrm{d}x=(d_{11}+d_{10})\,\delta'-(d_{11}^2-d_{10}^2). \tag{3.9}$$

Equations (3.7)–(3.9) provide a relationship between c_1 and d_{11}.

The assumptions (i)–(iii) are equivalent to those made by Yih & Guha (1955), Houghton & Isaacson (1970), Long (1970, 1974) and Su (1976). Chu & Baddour (1977) and Wood & Simpson (1984) have queried the validity of these assumptions because they imply that the contracting layer gains energy without associated work being done on it. They suggested that instead of (3.8) a conservation-of-energy equation be used for the contracting layer (the lower one in the present case), since little mixing is observed in this layer. The results obtained by using this assumption are very similar to those obtained from (3.7)–(3.9) over the range of parameters for which experimental observations were made (differences were less than 3%), and the observations could not distinguish between them. We will use (3.7)–(3.9) here.

If we define

$$\left.\begin{aligned} r = \frac{d_{10}}{D}, \quad s = \frac{\rho_1}{\rho_2}, \quad R = \frac{d_{11}}{d_{10}}, \quad \delta = \frac{\delta'}{d_{10}}, \\ F_{10}^2 = \frac{u_0^2}{(s^{-1}-1)\,g d_{10}}, \quad \Gamma^2 = \frac{c_1^2}{(s^{-1}-1)\,g d_{10}}, \end{aligned}\right\} \tag{3.10}$$

(3.7)–(3.9) may be written

$$\begin{aligned}(F_{10}+\Gamma)^2\Big\{r(1-r)\,(R-1-\delta)+\frac{R-1}{R(R+1)}(2-r(1+R-\delta))\,(1-rR+r\delta) \\ -\frac{r(1-s)\,(R-1)^2}{R(R+1)}(3-r-2rR+r\delta)\Big\} \\ = s(R-1)\,(1-rR)\,\{1-[r(1+R)]\}, \end{aligned} \tag{3.11}$$

$$\delta = \frac{2(1-s)\,(R-1)}{sR(R+1)}(F_{10}+\Gamma)^2. \tag{3.12}$$

These equations specify a unique jump speed as a function of its height. This relationship shown in figure 7 for various r-values, where the ordinate is the actual jump speed u_0+c_1 divided by c_0, the speed of long small-amplitude waves in this two-layer system with a free surface. c_0 is given by

$$c_0^2 = \tfrac{1}{2}gD\{1-(1-4(1-s)\,r(1-r))^{\frac{1}{2}}\}, \tag{3.13}$$

and we have

$$u_0+c_1 \to c_0 \quad \text{as} \quad d_{11} \to d_{10}, \tag{3.14}$$

i.e. infinitesimal jumps travel at the linear long-wave speed.

Although jumps conserve momentum they involve a loss of energy between the upstream and downstream states. Mechanisms for this energy loss are discussed in the next section. The rate of energy loss in the jump may be readily calculated from (3.1) and (3.2) and is given by (e.g. Su 1976)

$$\begin{aligned}\frac{\mathrm{d}E_{\mathrm{J}}}{\mathrm{d}t} &= \text{energy flux downstream} - \text{energy flux upstream} \\ &= \tfrac{1}{2}(u_0+c_1)^3\left\{\rho_1 d_{10}\, e\left(\frac{d_{11}}{d_{10}}-1\right)+\rho_2 d_{20}\, e\left(\frac{d_{21}}{d_{20}}-1\right)\right\}, \end{aligned} \tag{3.15}$$

where E_{J} denotes the energy in a region of fluid containing the jump,

$$e(x) = -\frac{x^3}{(1+x)^2\,(2+x)}, \tag{3.16}$$

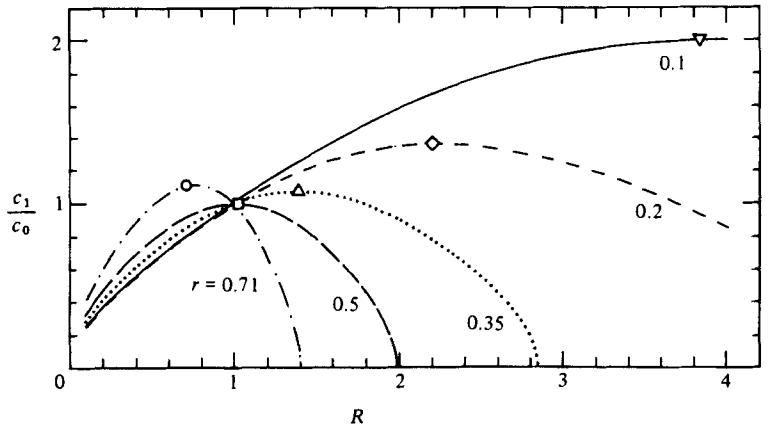

FIGURE 7. Bore speed as a function of height from (3.11) and (3.12) expressed in terms of the linear long-wave speed c_0 (3.13). The marks denote the points at which energy loss $dE_J/dt = 0$.

and for the above jump solutions to be valid we require

$$\frac{dE_J}{dt} < 0. \tag{3.17}$$

For each curve shown in figure 7 this condition is satisfied to the left of the symbol, which is just to the left of the peak of the curve. Hence the jump solutions are only possible on the rising branch of each curve.

For the assumed flow state 3C as depicted in figure 6, the flow downstream of the jump will be steady in a frame of reference moving with the obstacle. Accordingly, from (3.3) Bernoulli equations for each layer may be obtained in the form

$$\left.\begin{aligned} \tfrac{1}{2}u_1^2 + g(d_1+d_2) + \frac{p_s}{\rho_1} &= \text{const} = \tfrac{1}{2}u_{11}^2 + g(d_{11}+d_{21}), \\ \tfrac{1}{2}u_2^2 + g\left(\frac{\rho_1}{\rho_2}d_1 + d_2\right) + \frac{p_s}{\rho_2} &= \text{const} = \tfrac{1}{2}u_{21}^2 + g\left(\frac{\rho_1}{\rho_2}d_{11} + d_{21}\right). \end{aligned}\right\} \tag{3.18}$$

When the fluid is beneath the obstacle we have

$$u_1 = u_{11}\frac{d_{11}}{d_1}, \quad u_2 = u_{21}\frac{d_{21}}{d_2}, \quad d_2 = D - h(x) - d_1. \tag{3.19}$$

Subtracting to eliminate the pressure p_s, we obtain

$$\frac{\rho_2 u_{21}^2 d_{21}^2}{2(D-h-d_1)^2} - \frac{\rho_1 u_{11}^2 d_{11}^2}{2d_1^2} + (\rho_2-\rho_1)g(D-h-d_1) = \tfrac{1}{2}\rho_2 u_{21}^2 - \tfrac{1}{2}\rho_1 u_{11}^2 + g(\rho_2-\rho_1)d_{21}, \tag{3.20}$$

where all terms are constants apart from $d_1(x)$ and $h(x)$. Differentiating with respect to x then gives

$$\frac{dh}{dx}\left\{\frac{\rho_2 u_{21}^2 d_{21}^2}{(D-h-d_1)^3} - (\rho_2-\rho_1)g\right\} + \frac{dd_1}{dx}\left\{\frac{\rho_2 u_{21}^2 d_{21}^2}{(D-h-d_1)^3} + \frac{\rho_1 u_{11}^2 d_{11}^2}{d_1^3} - (\rho_2-\rho_1)g\right\} = 0. \tag{3.21}$$

Hence, where $\mathrm{d}h/\mathrm{d}x = 0$ (i.e. at the obstacle crest) we must have either

$$\frac{\mathrm{d}d_1}{\mathrm{d}x} = 0 \tag{3.22}$$

or

$$\frac{\rho_2 u_{21}^2 d_{21}^2}{(D-h_{\max}-d_{1c})^3} + \frac{\rho_1 u_{11}^2 d_{11}^2}{d_{1c}^3} - (\rho_2-\rho_1)\, g = 0, \tag{3.23}$$

where d_1 satisfying (3.23) is denoted by d_{1c}. Equation (3.22) applies for flow types 1A and 2B (subcritical and supercritical flow, where $d_{11} = d_{10}$), and (3.23) applies for type 3C. Equation (3.23) is equivalent to the statement that a local Froude number defined by

$$F_r \equiv \frac{u_0}{c_r} = 1, \tag{3.24}$$

where c_r is the linear long-wave speed in the two-layer shear flow between rigid boundaries. If we define

$$R_c = \frac{d_{1c}}{d_{10}}, \quad H = \frac{h_{\max}}{d_{10}}, \tag{3.25}$$

(3.20) and (3.23) may be written

$$\frac{1}{2s}\left\{\frac{(F_{10}+\Gamma)(1-r)}{1-rR+r\delta} - \Gamma\right\}^2 \left\{\left(\frac{1-rR+r\delta}{1-rH-rR_c}\right)^2 - 1\right\} - \frac{1}{2}\left\{\frac{F_{10}+\Gamma}{R} - \Gamma\right\}\left\{\left(\frac{R}{R_c}\right)^2 - 1\right\}$$
$$= H + R_c - R + \delta, \tag{3.26}$$

$$\frac{1}{s}\left\{\frac{(F_{10}+\Gamma)(1-r)}{1-rR+r\delta} - \Gamma\right\}^2 \frac{(1-rR+r\delta)^2 r}{(1-rH-rR_c)^3} + \left(\frac{F_{10}+\Gamma}{R} - \Gamma\right)^2 \frac{R^2}{R_c^3} = 1. \tag{3.27}$$

Equations (3.11), (3.12), (3.26) and (3.27) may be solved simultaneously to yield Γ, R and R_c as functions of F_{10} and H, for flow type 3C. Flow type 3D is demarcated by the line $R_c = 0$; the boundaries of regions 1A and 2B are given (in part) by (3.26) and (3.27), but with the upstream jump absent, so that in these equations $R = 1$, $\delta = 0$, $\Gamma = 0$.

In the region of blocked flow of the upper layer we have

$$u_{11} = 0, \tag{3.28}$$

so that, from continuity,

$$F_{10} + \Gamma = \Gamma R. \tag{3.29}$$

R and Γ are given by (3.11), (3.12) and (3.29), and are independent of H.

Regions in the (F_{10}, H)-plane where the various flow types of figure 4 may be found, according to this theoretical model, are shown in figure 8 for various values of r. The pattern of curves for small r resembles that for $r = 0$, as expected. Because of the hybrid nature of the system under study here, the curves denoting the limit of subcritical flow (type 1A) and the onset of type 3C flow are not quite coincident. The difference is very small, and the structure near point A' is actually as shown in figure 9, for values of r up to $r \approx 0.35$. This difference occurs because the upper surface is free except at the obstacle, where it is rigid. The nature of the flow in the various regions is fairly obvious except in the region $a'c'd'$, where it presumably has the character shown in the inset – a bore develops on the forward face of the obstacle but cannot propagate upstream. The regions $a'c'd'$ and $b'c'e'$ are both too small to be identified in these experiments, and we will ignore their presence in the rest

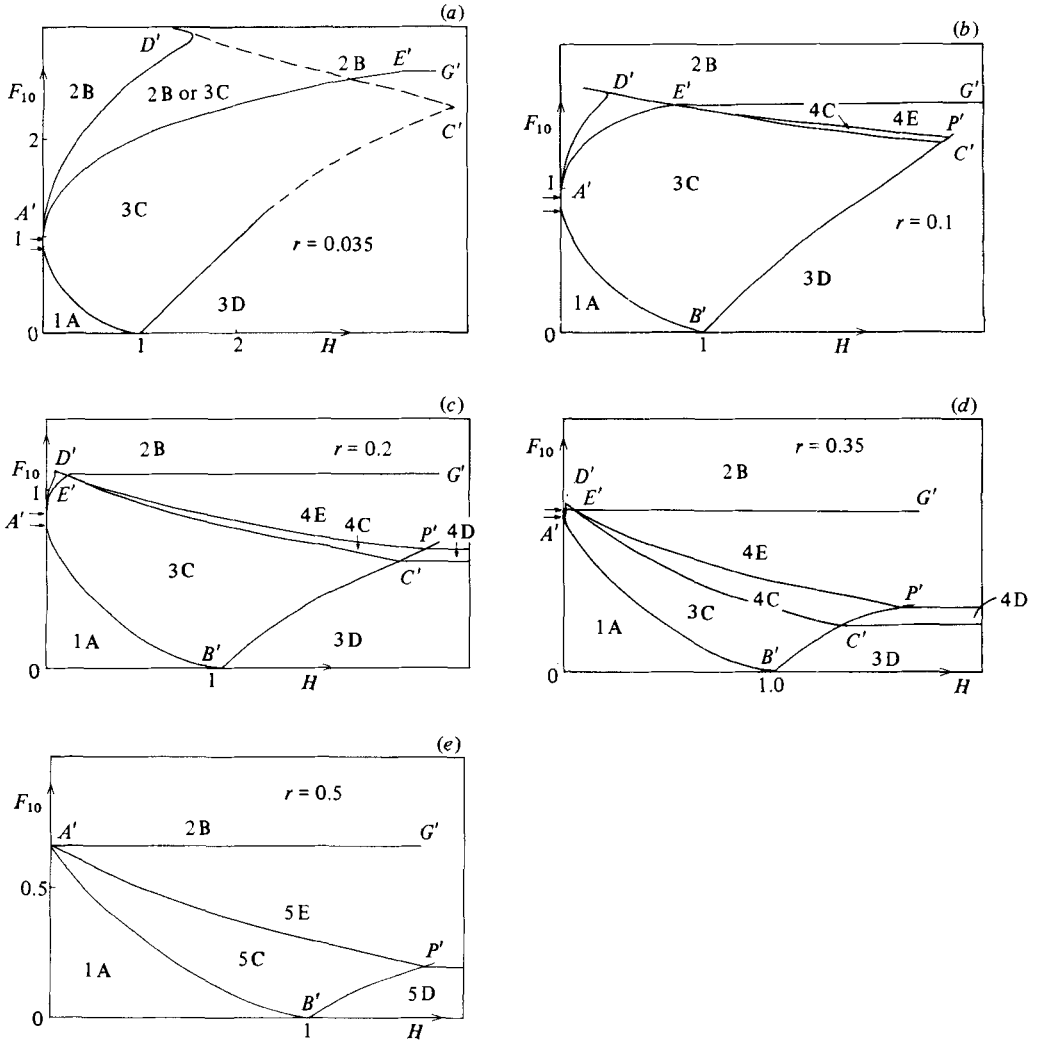

FIGURE 8. Flow-regime diagrams in terms of F_0 and H for various values of r. The dashed lines represent approximate locations of the boundaries, and the two arrows on the ordinate axis denote the points a' and b' of figure 9.

of this paper. It should be noted, however, that it would be quite a simple matter to construct a system in which these regions are significant.

In figure 8(a) the lower boundary of supercritical flow is given by curve $A'E'G'$. $A'E'$ is given by (3.26) and (3.27) with $R = 1$, $\delta = \Gamma = 0$, and the solution to these equations has a second branch which meets $A'E'$ in a cusp at E' (see Long 1954, figure 22). This second branch has larger values of R_c than does $A'E'$, and is not physically relevant. If we denote the Froude numbers at A' and E' by $F_{A'}$ and $F_{E'}$ respectively, for flows with $F_{A'} < F_{10} < F_{E'}$ the flow may be supercritical if H is to the left of $A'E'$. For $F_{10} > F_{E'}$ the flow will remain supercritical regardless of the height of the obstacle; hence the boundary $E'G'$ is horizontal at $F_{10} = F_{E'}$. As for single-layer flows, both supercritical and partially blocked flows are possible between curves $A'D'$ and $A'E'$; this region is discussed further in §5.

On the subcritical boundary $A'B'$ we have $R = 1$ and $\mathrm{d}E_J/\mathrm{d}t = 0$. As F and/or H increase above this line the energy loss across the jump at first increases, and then

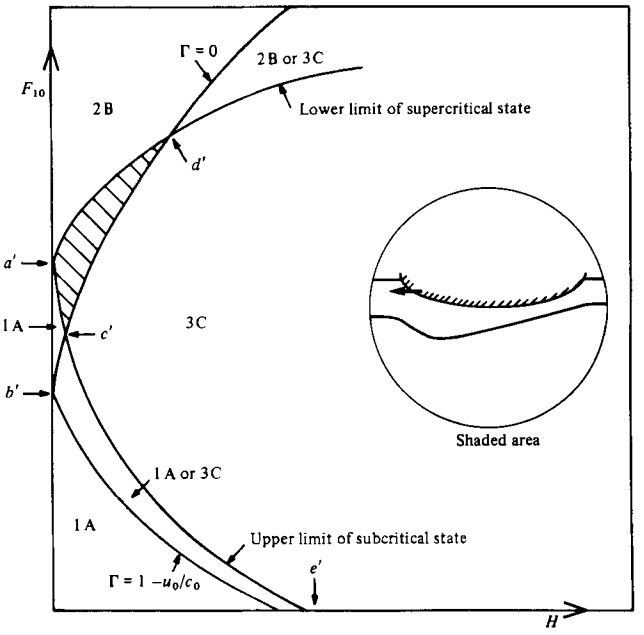

FIGURE 9. Schematic detailed structure of figures 8(*a–d*) near point *A'*.

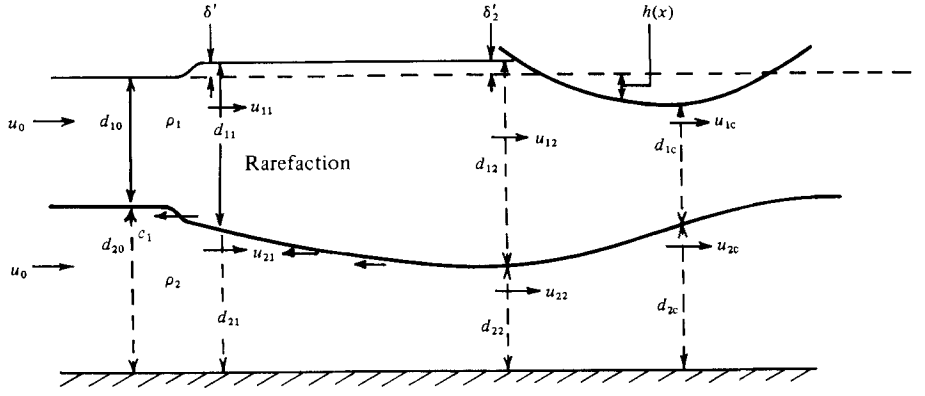

FIGURE 10. Notation for flow types 4C and 5C, with axes fixed relative to the obstacle.

decreases to zero as the line $D'C'$ is reached. Beyond this line state 3C is no longer possible because the assumed upstream jump will not satisfy the energy criterion. Instead, guided by the observations, we assume a model as shown in figure 10, where the upstream motion consists of a (possible) upstream jump with $\mathrm{d}E_J/\mathrm{d}t = 0$, followed by a time-dependent rarefaction region. In the latter, the leading part of the rarefaction travels faster than the trailing part, so that this region becomes increasingly extended as time progresses. For larger values of r (e.g. $r = 0.5$) the initial zero-energy-loss jump may be absent.

In order to calculate the properties of flow types 4C, 4D, 5C, 5D we first make use of the theory of hyperbolic equations and simple waves (Houghton & Isaacson 1970) to relate conditions across the rarefaction. Equations (3.1*a*) and (3.3) may be written

$$\boldsymbol{v}_t + \boldsymbol{C}\boldsymbol{v}_x = \boldsymbol{0}, \tag{3.30}$$

where suffixes x and t denote derivatives, and

$$\boldsymbol{v} = \begin{pmatrix} u_2 \\ d_2 \\ u_1 \\ d_1 \end{pmatrix}, \quad \boldsymbol{C} = \begin{pmatrix} u_2 & g & 0 & gs \\ d_2 & u_2 & 0 & 0 \\ 0 & g & u_1 & g \\ 0 & 0 & d_1 & u_1 \end{pmatrix}, \quad \boldsymbol{0} = \begin{pmatrix} 0 \\ 0 \\ 0 \\ 0 \end{pmatrix}. \tag{3.31}$$

The roots $\lambda_i(x,t)$, $i = 1, \ldots, 4$ of the characteristic equation of the matrix $\boldsymbol{C}$

$$\det(\boldsymbol{C} - \lambda \boldsymbol{I}) = 0, \tag{3.32}$$

where $\boldsymbol{I}$ is the identity matrix, determine the characteristic curves $x = x(t)$ as solutions of

$$\frac{\mathrm{d}x}{\mathrm{d}t} = \lambda_i(x,t) \quad (i = 1, \ldots, 4). \tag{3.33}$$

These λ_i are the linear wave speeds for given u_1, u_2, d_1 and d_2. If these are ordered so that

$$\lambda_1 \leqslant \lambda_2 \leqslant \lambda_3 \leqslant \lambda_4,$$

λ_1 and λ_4 represent surface or external waves, and λ_2 and λ_3 the internal waves. λ_2 is negative and denotes the velocity of an internal wave moving to the left. Equation (3.32) becomes

$$\left(1 - \frac{(\lambda - u_1)^2}{d_1 g}\right)((1-s)\, g d_1 d_2 - d_1(\lambda - u_2)^2) - s d_2 (\lambda - u_1)^2 = 0. \tag{3.34}$$

On a characteristic $x = x(t)$ we may write

$$\dot{\boldsymbol{v}} \equiv \frac{\mathrm{d}}{\mathrm{d}t}\boldsymbol{v}(x(t), t) = \boldsymbol{v}_x \lambda_i + \boldsymbol{v}_t, \tag{3.35}$$

which with (3.30) becomes

$$(\boldsymbol{C} - \lambda_i \boldsymbol{I})\, \boldsymbol{v}_x = \dot{\boldsymbol{v}}. \tag{3.36}$$

Each component of the vector $\dot{\boldsymbol{v}}$ is therefore a linear combination of the components of the vector $\boldsymbol{v}_x$. Hence we may obtain relationships between the variables by replacing the fourth (or any other) column of $\boldsymbol{C} - \lambda_i \boldsymbol{I}$ by $\dot{\boldsymbol{v}}$ and equating the determinant of the resulting matrix to zero. Our object is to relate conditions downstream of the rarefaction to those upstream, and the rarefaction or expansion may be regarded as a simple wave (i.e. a disturbance moving into uniform conditions and propagating on one family of characteristics only) behind the zero-energy-loss jump. The simple wave propagates along the characteristics $\mathrm{d}x/\mathrm{d}t = \lambda_2$; accordingly the other families of characteristics relate conditions across this wave, and we obtain

$$\frac{\mathrm{d}d_2}{\mathrm{d}t} g d_1 (u_2 - \lambda_i) + \frac{\mathrm{d}d_1}{\mathrm{d}t}(u_1 - \lambda_i)((u_2 - \lambda_i)^2 - g d_2)$$

$$- \frac{\mathrm{d}u_2}{\mathrm{d}t} g d_1 d_2 - \frac{\mathrm{d}u_1}{\mathrm{d}t} d_1((u_2 - \lambda_i)^2 - g d_2) = 0 \quad (i = 1, 3, 4) \tag{3.37}$$

on $\mathrm{d}x/\mathrm{d}t = \lambda_i$. With reference to figure 10, if we define

$$\left.\begin{aligned} V_1 &= \frac{u_{12}}{\left(g\frac{\Delta\rho}{\rho_1}d_{10}\right)^{\frac{1}{2}}}, \quad V_2 = \frac{u_{22}}{\left(g\frac{\Delta\rho}{\rho_1}d_{10}\right)^{\frac{1}{2}}}, \\ R_1 &= \frac{d_{12}}{d_{10}}, \quad R_2 = \frac{d_{22}}{d_{10}}, \quad \Gamma_k = \frac{\lambda_k}{\left(g\frac{\Delta\rho}{\rho_1}d_{10}\right)^{\frac{1}{2}}} \quad (k = 1, \ldots, 4), \end{aligned}\right\} \tag{3.38}$$

and take R_1 as the independent variable, (3.37) may be written

$$\frac{\mathrm{d}V_2}{\mathrm{d}R_1}R_1R_2 - \frac{\mathrm{d}R_2}{\mathrm{d}R_1}R_1(V_2-\Gamma_k) + \frac{\mathrm{d}V_1}{\mathrm{d}R_1}R_1\left(\left(\frac{1}{s}-1\right)(V_2-\Gamma_k)^2 - R_2\right)$$
$$= (V_1-\Gamma_k)\left(\left(\frac{1}{s}-1\right)(V_2-\Gamma_k)^2 - R_2\right) \quad (k = 1, 3, 4). \tag{3.39}$$

From (3.34) the Γ_k are given by

$$\left(\frac{R_1 s}{1-s} - (\Gamma_k - V_1)^2\right)(sR_2 - (\Gamma_k - V_2)^2) - \frac{s^2R_2}{1-s}(\Gamma_k - V_1)^2 = 0. \tag{3.40}$$

Equation (3.39) may be integrated across the rarefaction to give V_1, V_2 and R_2 as functions of R_1. The relations so obtained are analogous to Riemann invariants in a single-layer system. To complete the system, the equation relating conditions downstream of the rarefaction to conditions at the obstacle crest, and the equation for the critical condition at the crest are required (corresponding to (3.26) and (3.27) respectively), and these are

$$\tfrac{1}{2}V_2^2\left(\frac{R_2^2}{\left(\frac{1}{r}-H-R_c\right)^2}-1\right) - \tfrac{1}{2}sV_1^2\left(\frac{R_1^2}{R_c^2}-1\right) = s\left(H+R_c+R_2-\frac{1}{r}\right), \tag{3.41}$$

$$\frac{1}{s}\frac{V_2^2R_2^2}{\left(\frac{1}{r}-H-R_c\right)^3} + \frac{V_1^2R_1^2}{R_c^3} = 1. \tag{3.42}$$

In summary, to establish the flow field of figure 10 for given F_{10} and H, we need to (i) solve for the limiting ($\mathrm{d}E_J/\mathrm{d}t = 0$) jump with (3.11) and (3.12) if it is present; (ii) integrate the differential equations (3.39) to obtain V_1, V_2 and R_2 as functions of R_1, and then (iii) solve these equations simultaneously with (3.41) and (3.42) to obtain R_1 and R_c. This has been done for all the values of r shown in figure 8.

As F_{10} and/or H are increased further so that the upstream disturbance is increased, a point is reached where this motion becomes just critical immediately upstream of the obstacle. This gives the maximum upstream disturbance possible, and it is not altered by further increases in F_{10} and/or H. With critical flow just upstream, the flow over the obstacle must now be supercritical; the critical condition (3.24) cannot be satisfied, and the flow at the obstacle crest satisfies (3.22). From observations, the flow then adjusts to downstream reality by passing through a hydraulic drop on the lee side of the obstacle, giving flow types 4E, 5E and also 2F. The calculation of flow parameters in these regimes is substantially more complicated than for those described above, since it is now necessary to solve for the complete time-dependent

flow (i.e. downstream as well as upstream), utilizing the appropriate relations across downstream jumps, drops and rarefactions, and the original conditions far downstream. This has been done for a single-layer flow by Houghton & Kasahara (1969), but is not attempted here. The properties of hydraulic drops are discussed in more detail in §6.

4. Upstream jumps and undular bores

Upstream jumps, frequently in the form of undular bores, are common features of these flows, and in many cases the upstream bore is the most conspicuous phenomenon present. In this section we discuss the properties of these internal bores *per se*, before we proceed in §5 to a comparison between the overall properties of the observed flows and the theory of §3.

Examples of the types of bores observed are shown in figures 5 (*a*, *b*) and 11. For all values of r for which bores were found (0.035, 0.1, 0.2, 0.35), for sufficiently small amplitudes the bore was wholly laminar (e.g. figure 11*b*). For $r = 0.035$, 0.1 and 0.2 a train of waves with amplitude decreasing monotonically to zero downstream (at the new interface elevation) was evident downstream of the bore front. The amplitudes of these wavetrains generally decreased as r increased, and the waves were barely discernible for $r = 0.35$. In all experiments this pattern of waves appeared to be steady, once it was established, and no variation in bore speed could be detected within 1 %. For $r = 0.035$, 0.1 and 0.2, the bore amplitude, speed and wave amplitude all increased with increasing R, until a point was reached where turbulence appeared at the interface. This instability first occurred on the leeside of the first wave 'crest' and is evident in figure 5(*a*), where it is marginally turbulent. At larger amplitudes the turbulent region extended from the 'crest' down the whole leeside of the first wave, tended to become laminar again on the forward face of the second wave, was turbulent again on the leeside and so on, decreasing with the wave amplitude (figure 5*b*, 11*a*). At even larger amplitudes the flow behind the leading crest became fully turbulent (figure 11*c*), and the flow resembled a gravity current with the initial wave crest as the gravity current head; subsequent waves were barely distinguishable. In all cases, however, the forward face of the bore was always laminar. For $r = 0.35$ no turbulence was observed, and the bore mainly consisted of a forward face which propagated without discernible change in shape.

Figure 12 shows the observed bore propagation speeds (c/c_0 or $F+\Gamma$) versus bore height $R-1$ for $r = 0.035$, 0.1, 0.2 and 0.35, together with the theoretical curves from (3.11). The bores are observed to move at slightly slower speeds than those expected from the inviscid hydrostatic theory. For $r = 0.035$, 0.1 and 0.2, the point at which the bore changes from laminar to 'turbulent' is marked; beyond this point the bore speed increases more slowly with R than for the laminar bores, and for $r = 0.1$, 0.2 there appeared to be almost no increase at all.

Long (1974) described experiments with $r = 0.2, s = 0.9$, where a similar discrepancy was found between these theoretical bore speeds and the observed ones, over a range of R-values. Yih & Guha (1955) reported observations of bores between two immiscible fluids where one layer was at rest relative to the bore, or both layers had the same velocity downstream of it. Because of the different situations it is not possible to make a direct comparison between their results and those described here, but a similar discrepancy between the hydrostatic theory and observation was reported.

Although internal bores are quite common in geophysical flows, to my knowledge

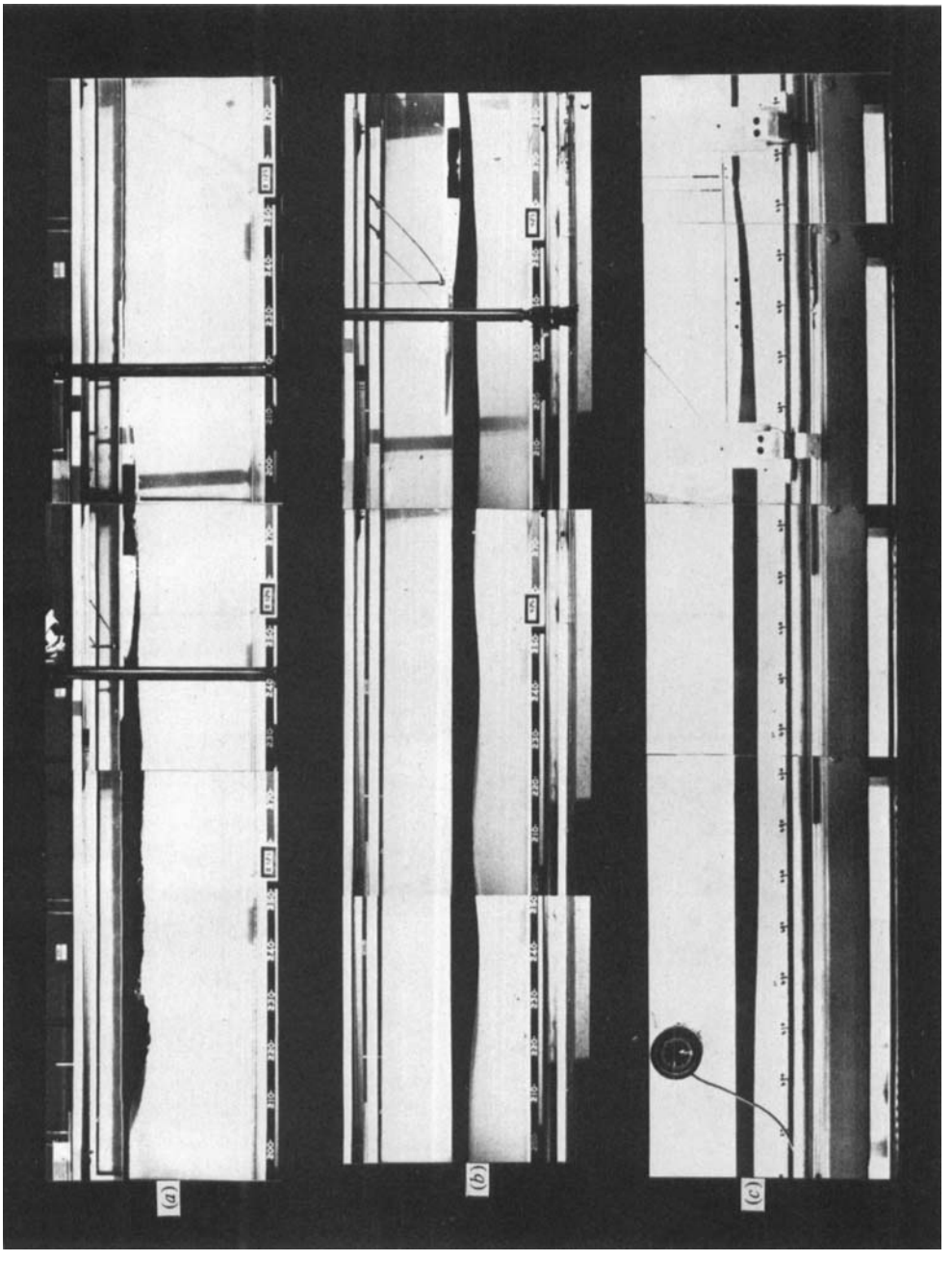

FIGURE 11. Examples of upstream bores. (*a*) A large-amplitude turbulent bore, $r = 0.035$. (*b*) A laminar bore, $r = 0.2$. (*c*) A laminar bore with $\mathrm{d}E_1/\mathrm{d}t = 0$, $r = 0.035$.

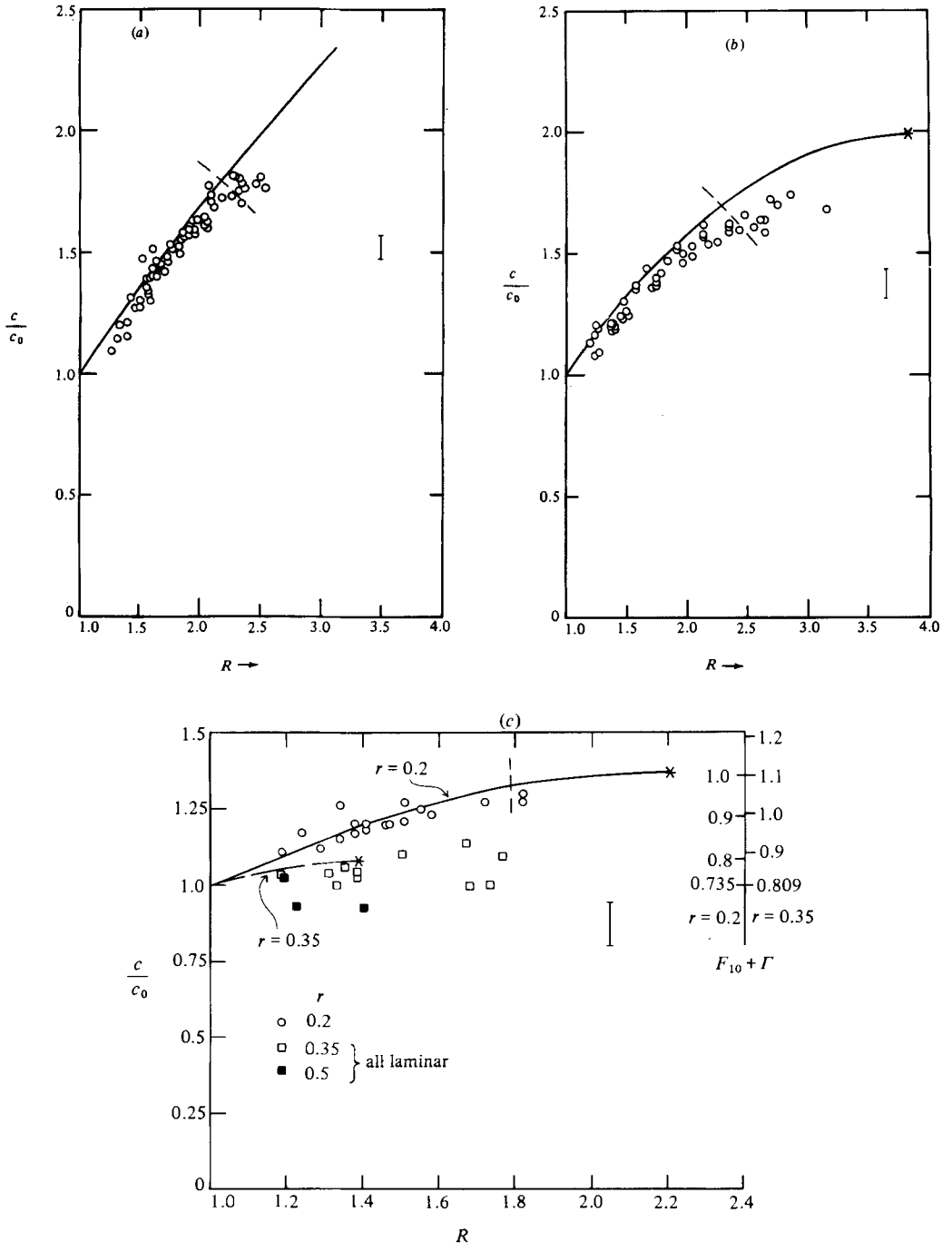

FIGURE 12. Bore speeds as a function of jump height – a comparison between hydrostatic theory and observations. (*a*) $r = 0.035$; (*b*) 0.1; (*c*) 0.2, 0.35, 0.5. Asterisks denote the points where $dE_J/dt = 0$. The dashed lines denote the observed boundaries between laminar and turbulent upstream motion. For $r = 0.5$ the upstream motiom is not a bore, but the points denote the observed speed.

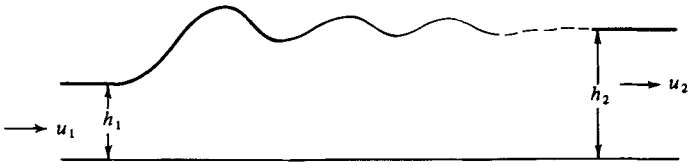

FIGURE 13. Schematic diagram of a laminar bore in a single-layer system.

detailed laboratory observations of them have not previously been described in the literature, and we next discuss the reasons for their observed character. The nature of bores in the simpler single-layer system has received much more study than the more complex two-layer system, but even now single-layer (free-surface) bores are not completely understood. Before discussing two-layer bores, however, we first summarize the state of knowledge of single-layer bores.

Bores in single-layer systems

We may loosely define a bore as the transition region between one uniform stream and another, in a steady state. A typical observed laminar free-surface bore is shown schematically in figure 13; the flow pattern is steady and, taking axes moving with the bore, the flow upstream is supercritical ($F = u_1/(gh_1)^{\frac{1}{2}} > 1$) and the flow downstream is subcritical ($F = u_2/(gh_2)^{\frac{1}{2}} < 1$). Benjamin & Lighthill (1954) have shown that bores may be suitably described in terms of the three quantities Q^*, R^* and S^*, where Q^* is the volume flow rate per unit span, R^* is the energy per unit mass (i.e. g times the total head) and S^* is the flow force (the total momentum flow rate (i.e. inluding pressure) per unit span, divided by density). For a uniform stream of speed u_1 and depth h_1, Q^*, R^* and S^* have the forms

$$Q^* = u_1 h_1, \quad R^* = \tfrac{1}{2}u_1^2 + gh_1, \quad S^* = u_1^2 h_1 + \tfrac{1}{2}gh_1^2, \tag{4.1}$$

which for the case of figure 13 correspond to the upstream values. Benjamin & Lighthill show that (in all probability) the values of Q^*, R^* and S^* determine a unique train of stationary finite-amplitude gravity waves, specifying implicitly their depth, amplitude and wavelength. They also show that inviscid bores, where there is a transition from a uniform stream to a wavetrain which has the same values of Q^*, R^* and S^*, are not possible – the only possible solution in this case is a solitary wave. Peregrine (1966) and Fornberg & Whitham (1978) describe the results of numerical studies of the temporal development of inviscid bores from initial states of gradual change (Peregrine) and abrupt change (Fornberg & Whitham) from one uniform stream to another. These systems evolve into undular bores with oscillations which decrease downstream, but steady state is not attained, and these authors conclude that in an inviscid system the initial wave crest (which has largest amplitude) eventually detaches and propagates ahead as a solitary wave, to be eventually succeeded by the second crest, and so on. It appears therefore that the final state of the inviscid bore is an unsteady structure resulting in the continuous production of a succession of solitary waves. Peregrine also describes how the undulations are formed by pressure effects resulting from the non-hydrostatic components of the flow.

Inviscid bores do not occur in practice. If a small amount of energy dissipation takes place at or near the front face of the bore (for example, by turbulence associated with a breaking initial wave), R^* is decreased but Q^* and S^* are unchanged in value, and a transition from a uniform stream to a finite-amplitude (cnoidal for long waves) wavetrain may occur. If instead R^* progressively decreases downstream down the

wavetrain for some reason, the waves become sinusoidal and their amplitude falls to zero. The situation with real bores is, however, slightly different. Sturtevant (1965) has shown that, for a bore moving into fluid at rest (as in figure 13), R^* and S^* *increase* as the bore is traversed, because the lower boundary exerts a stress on the deeper fluid in the downstream direction (in the frame of the bore). Byatt-Smith (1971) has investigated this effect of a bottom viscous boundary layer in some detail, and has obtained realistic steady, spatially decaying undular bore solutions. R^* and S^* both increase, and the wave amplitudes decrease, as one moves downstream from the bore front. For larger bores the waves may break and bottom boundary layers may become turbulent, but the same processes still apply. This then is the general character of a bore advancing into still water over a rigid boundary.

Internal bores in a two-layer system

This subject is much less well developed than that for single-layer flows. For *purely hydrostatic* flows, the flow of a single active lower layer below an infinitely deep upper layer may be described by the same equations as for a single layer *per se*, if g is replaced by $g\Delta\rho/\rho_2$. However, for flows with shorter lengthscales, where horizontal gradients become important so that the flow is not hydrostatic, we cannot make this identification. The above results for single-layer systems are related to the fact that small-amplitude long surface waves satisfy the Korteweg–de Vries equation. Benjamin (1966) showed that small-amplitude wave motion in a stratified or two-layer system where the wavelength was much greater than the total depth was also described by a Korteweg–de Vries equation, but that waves in a system where the upper (or lower) layer was infinitely deep satisfy a different equation now known as the Benjamin–Ono equation (Benjamin 1967; Ono 1975). The latter has since been generalized to fluids of finite total depth, but still with a shallow (layer depth $\ll$ wavelength) lower or upper layer – the 'finite-depth' or 'intermediate-long-wave' (ILW) equation (Joseph 1977; Kubota, Ko & Dobbs 1978).

There is currently no known nonlinear equation governing small-amplitude long internal waves that is formally valid over the whole range of depths for two-layer systems. It also appears that, in circumstances where the 'finite-depth' or ILW limit is applicable, a slightly different representation of the equation is required to describe periodic waves from that for solitary waves (Ablowitz *et al.* 1982).

Recent experiments by Koop & Butler (1981) and Segur & Hammack (1982) show that, for solitary waves, the Korteweg–de Vries equation is more accurate than the others in most cases and has the widest range of validity. Although the experiments were far from exhaustive, a parameter range for which the Benjamin–Ono equation is valid could not be found experimentally, and the range of validity for the finite-depth or ILW equation was disappointingly small and for restricted wave amplitudes. These conclusions indicate that, for the present purposes, it is appropriate to restrict the present discussion to the Korteweg–de Vries equation, and we follow the formalism of Benjamin (1966). However, we cannot expect this weakly nonlinear theory to apply quantitatively to all of the present experiments because, first, in many cases the bores have very large wave amplitudes and, secondly, the wavelength is often comparable to the total depth, particularly when r is small.

For steady flow in a stratified fluid of finite depth we define the total head H^* and the flow force S^* by

$$H^*(x,z) = p + \tfrac{1}{2}(u^2+w^2) + \rho g z, \tag{4.2}$$

$$S^*(x) = \int (p+\rho u^2)\,\mathrm{d}z = \int (H^* + \tfrac{1}{2}\rho(u^2-w^2) - \rho g z)\,\mathrm{d}z, \tag{4.3}$$

in the usual notation and in a frame of reference moving with the bore, where the integral is through the whole depth of the fluid. As for the single-layer case we consider the transition from a uniform flow to a periodic wavetrain, and denote the upstream conditions by a subscript zero. The rate of loss of energy in a jump or dissipation region between x_0 and x is given by

$$\frac{\partial}{\partial t}\int_{x_0}^{x} E\,\mathrm{d}x = \int u(x,z)\,H^*(x,z)\,\mathrm{d}z - \int u(x_0,z)\,H^*(x_0,z)\,\mathrm{d}z, \tag{4.4}$$

and this quantity is equal to $\mathrm{d}E_J/\mathrm{d}t$ (3.15) if the jump lies wholly between x_0 and x. We express the vertical displacement of streamlines from their upstream levels in the form

$$\zeta = f(x)\,\phi(z),$$

where $\phi(z)$ is the vertical eigenfunction for the lowest internal wave mode of infinite length. For a two-layer system of total depth D and upper depth d_{10} with a free surface, $\phi(z)$ is given by

$$\left.\begin{aligned} \phi &= \frac{z}{D-d_{10}} \quad (0 < z < D-d_{10}), \\ &= \frac{D-c_0^2/g-z}{d_{10}-c_0^2/g} \quad (D-d_{10} < z < D), \end{aligned}\right\} \tag{4.5}$$

where c_0 is the linear long wave speed given by (3.13).

For a periodic wavetrain with suitably long wavelength and small amplitude, Benjamin (1966) showed that $f(x)$ must satisfy

$$I\left(\frac{\mathrm{d}f}{\mathrm{d}x}\right)^2 = Jf^2 + Kf^3 + L, \tag{4.6}$$

where

$$I = c_0^2\int \rho\phi^2\,\mathrm{d}z, \quad J = (c^2-c_0^2)\int \rho\phi_z^2\,\mathrm{d}z, \quad K = -c_0^2\int \rho\phi_z^3\,\mathrm{d}z; \tag{4.7}$$

$\phi_z = \mathrm{d}\phi/\mathrm{d}z$, ρ is the fluid density and

$$L = 2\left(\int\left(\frac{u}{c}H^* - H_0^*\right)\mathrm{d}z - (S^*-S_0^*)\right). \tag{4.8}$$

Here the integrals are again over the total depth, c is the speed of propagation of the wavetrain and H_0^*, S_0^* denote the upstream values of H^*, S^* respectively. The first term in L is the energy-loss term (4.4) divided by the bore speed.

Equation (4.6) is a nonlinear differential equation of standard type, and the nature of its solutions may be inferred from figure 14 (following Benjamin 1966). I and J are positive quantities and K is positive for $r < 0.513$ (for $s = 0.79$), which covers all experimental cases under discussion. Changes in H^* and S^* only affect L. The cubic right-hand side of (4.6) has the form shown for various values of L, and solutions are possible where the function is positive. The flow force S^* is constant if there are no external forces acting on the fluid. For an internal bore on a shallow upper layer moving into fluid at rest there will be a slight decrease in S^* (below S_0^*) because of the stress at the bottom boundary acting on the lower layer, which has a net motion on the opposite direction to that of the bore after the bore front has passed. In the present experiments this effect is negligible if r is small, because of the remoteness of the lower boundary and the consequent small velocities there. This slight tendency to increase L is outweighed by a decrease in $\int uH^*\,\mathrm{d}z$, because of dissipation of kinetic

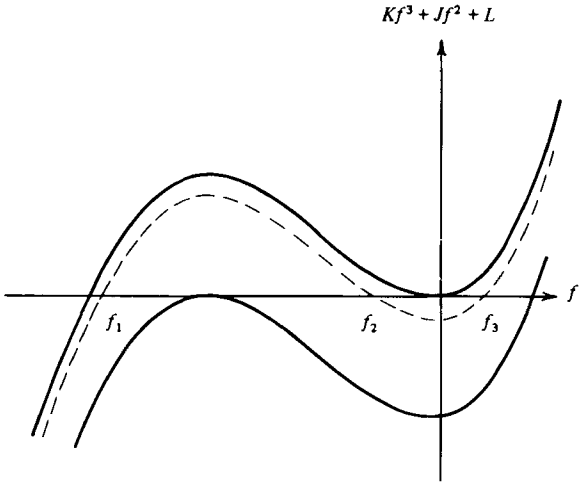

FIGURE 14. Graphs of the cubic equation that determines the character of the solutions of (4.6), for various values of L (4.8).

energy at the interface, which reduces $\int uH^* \,\mathrm{d}z$ but leaves S^* unchanged. The magnitude of this effect is estimated below for laminar bores, and will be even larger for turbulent bores, but for the present we merely note that the net effect results in a decrease of L below zero.

If $L = 0$, as for a purely inviscid bore, the only relevant solution of (4.6) is one representing a solitary wave of depression. This suggests, paralleling the single-layer case, that steady-state inviscid bores are not possible in two-layer or stratified finite-depth systems, and that attempts to set up such a bore will result in the continuous production of a sequence of solitary waves. This conjecture is far from proven, however. If a small decrease in L occurs at the bore front the cubic is lowered slightly and (4.6) admits a periodic cnoidal wave solution of large amplitude oscillating between the zeros f_1 and f_2. If L slowly decreases as one moves further downstream from the front, the waves tend to sinusoidal form and the wave amplitude decreases to zero as f_1 and f_2 coalesce. Further decrease in L only results in adjustments to the parallel flow. The interesting point is that very small changes in L may result in large changes in the wave structure.

This dynamical picture of the internal bores is qualitatively fully consistent with the observations described at the beginning of this section. If L decreases to the extent that the wave amplitude decreases to zero, the resulting change in interface height across the bore is given by

$$f = -\frac{2}{3}\frac{J}{K}. \tag{4.9}$$

From this we may obtain the expression

$$\left(\frac{c}{c_0}\right)^2 - 1 = \frac{3}{2}\frac{d_{10}\int \rho(-)\,\phi_z^3 \,\mathrm{d}z\,(R-1)}{\int \rho\phi_z^2 \,\mathrm{d}z\,(1-c_0^2/gd_{10})}, \tag{4.10}$$

where R is defined by (3.10), and

$$R - 1 = -f\Big/\left(d_{10}\left(1-\frac{c_0^2}{gd_{10}}\right)\right). \tag{4.11}$$

We may express (4.10) as

$$\frac{c}{c_0} = 1+\alpha(R-1)+O(R-1)^2, \tag{4.12}$$

where α is half the right-hand side of (4.10). Substituting from (4.5) and evaluating gives values for α which are the same as those from the 'jump' model (3.11), as expected (Su 1976).

In order to complete this description of the mechanics of the observed bores, we need to estimate the magnitude of the viscous effects. Interfacial and boundary stresses cause a progressive change in L (4.8), which results in a change in the internal waves. The calculation of this change in $L(x)$ has been relegated to the Appendix, where it is shown that the contribution of the interfacial and other boundary layers to $L(x)$ is given approximately by (A 9). The value L that is *required* in order to decrease the amplitude of the waves to zero is that required to lower the cubic of figure 14 from the uppermost curve to the lowest, according to the model of (4.6). This value is

$$L = -\frac{4}{27}\frac{J^3}{K^2} = -\tfrac{1}{2}d_{10}^3 c_0^2 \int \rho(-)\,\phi_z^3\,\mathrm{d}z \frac{(R-1)^3}{(1-c_0^2/gd_{10})^3}. \tag{4.13}$$

Equating (4.13) and (A 10) gives

$$\left(\frac{\nu_1 x}{c_0}\right)^{\frac{1}{2}} \approx \frac{1}{2}\frac{(R-1)^3}{g(R,r)\,(1-c_0^2/gd_{10})^3}\left(\left\{\frac{1}{1-c_0^2/gd_{10}}\right\}^3 - \frac{1}{s}\left\{\frac{r}{1-r}\right\}^2\right). \tag{4.14}$$

For R close to unity this relation may be satisfied for decay distances x that are comparable to those observed in the laboratory, for all relevant values of r. Hence we may conclude that viscous dissipation at the interface can account for the decrease in wave amplitude behind the bore. Note that the waves are *not* 'damped' in the usual sense of viscous damping, which applies (for example) to solitary waves. Instead, the decrease in wave amplitude is due to the changing character of the wavetrain caused by the changing value of L.

One possibility which could not be dismissed *a priori* is that the wave amplitude decays behind the bore because of an inviscid nonlinear interaction with the mean shear. If the flow is potentially unstable via shear instability, it is conceivable that a forced wave with suitable phase propagation (e.g. the bore undulations) could decay and lose its energy to the mean flow – a process that would correspond to a decaying eigenfunction with complex frequency. To test this possibility, the inviscid stability of the steady two-layer shear flow (uniform density and velocity in each layer) was examined, and the results compared with some representative observations. In every such case where an observed undular bore was laminar (see figure 12), the flow was found to be theoretically stable to disturbances that had the same wavelength; conversely, the flow was theoretically unstable for the same wavelengths as those of bores that were observed to be turbulent. Hence there was no indication of a wave–mean-flow interaction decay process other than the obvious one of turbulence due to Kelvin–Helmholtz instability.

5. Dependence of upstream effects on obstacle height: comparison with observations

In this section we compare the results obtained from the theoretical model of §3 with the observations. In an overall sense the agreement is quite reasonable; the boundaries of the various flow types obtained from the theory agree quite well with

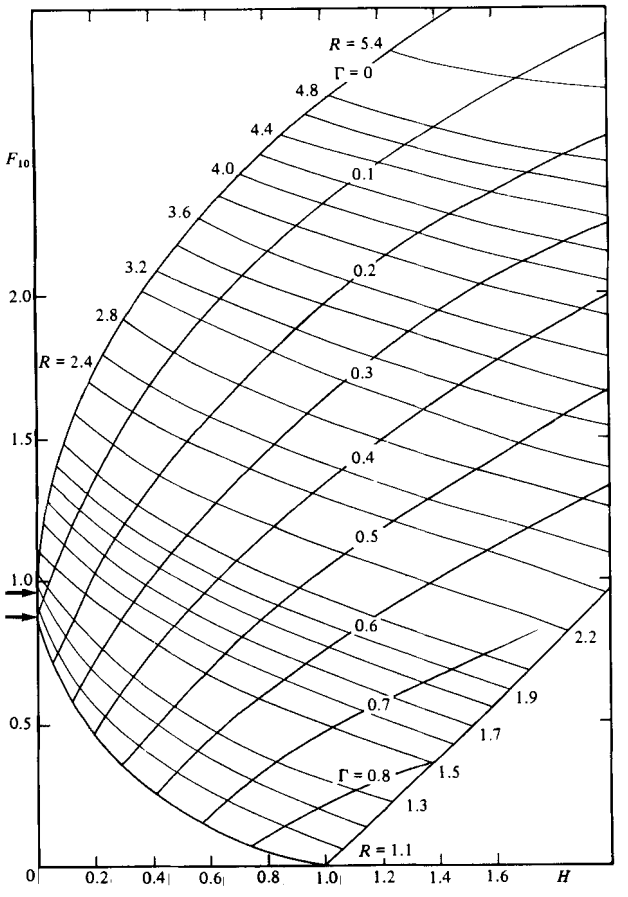

FIGURE 15. The curves Γ = constant, R = constant, giving the speed and amplitude of the upstream motion as functions of F_{10} and H, for $r = 0.035$. The overall pattern of the diagram is shown in figure 4.

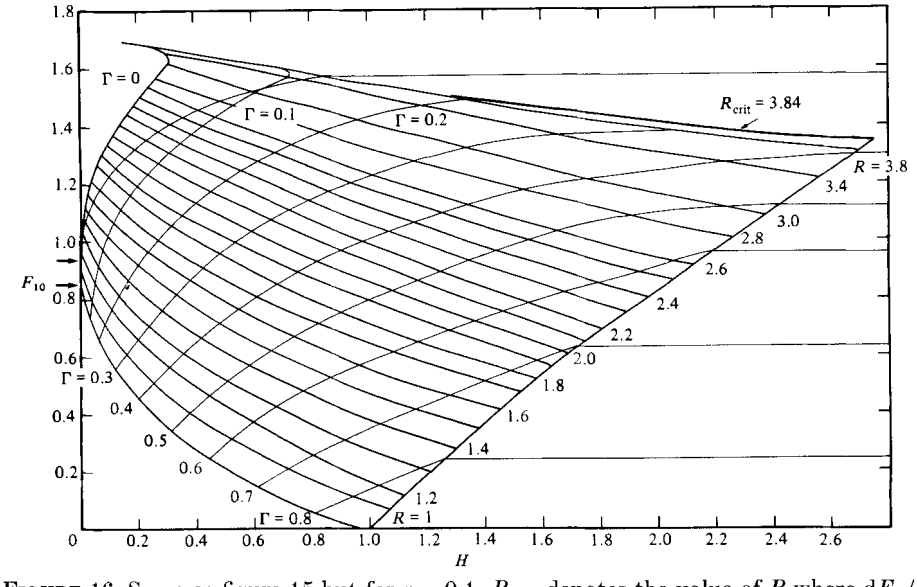

FIGURE 16. Same as figure 15 but for $r = 0.1$. R_{crit} denotes the value of R where $dE_J/dt = 0$.

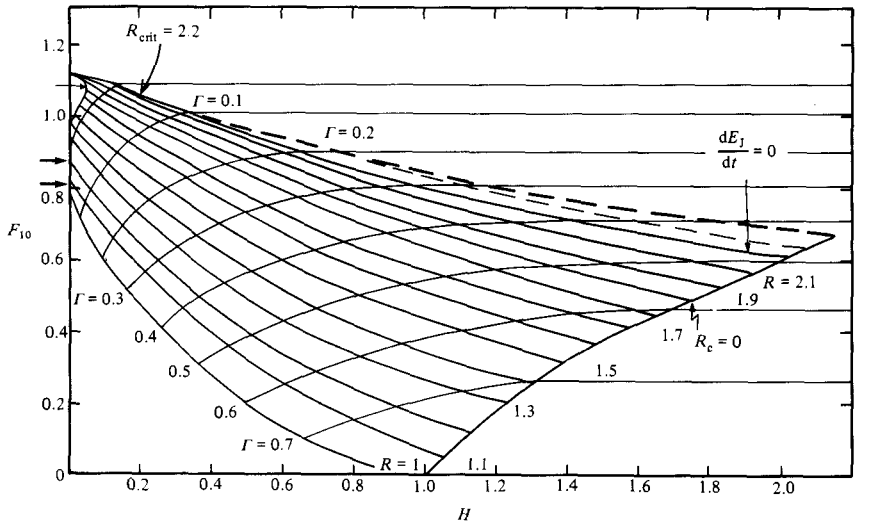

FIGURE 17. Same as figure 16 but for $r = 0.2$. The heavy dashed line denotes the upper limit of flow states where flow at the obstacle crest is critical.

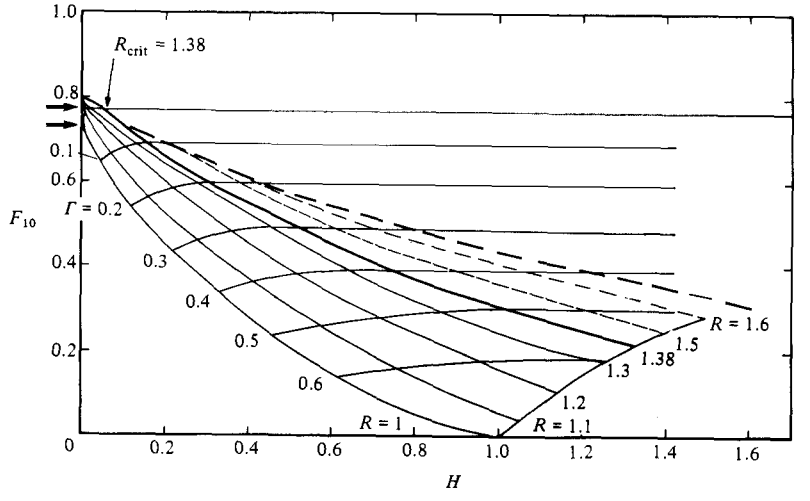

FIGURE 18. Same as figure 17 but for $r = 0.35$.

the observations, with a few exceptions which are discussed below. We consider the flows in order of increasing r.

From the inviscid equations of §3 the parameters Γ (relative bore speed) and R (bore amplitude) for the upstream motion may be computed as functions of F_{10} and H, and these are shown in figures 15–19 for the various values of r (these are the same diagrams as in figure 8 but with the added details). For $r = 0.035$ the pattern of R, Γ curves is very similar to that for the single-layer case ($r = 0$). In the regions of totally blocked flow of the upper layer, the Γ, R curves are horizontal so that Γ and R are independent of H – once the flow is totally blocked, a taller obstacle makes no difference to the upstream motion. At the upper limit of the region of 'pure' internal bores without rarefactions (line $E'C'$ of figure 8*b–d*) which is given by the criterion $dE_J/dt = 0$ across the upstream jump, the curves $\Gamma =$ constant are horizontal, reflecting the fact that this criterion is a property of the bore and not the obstacle

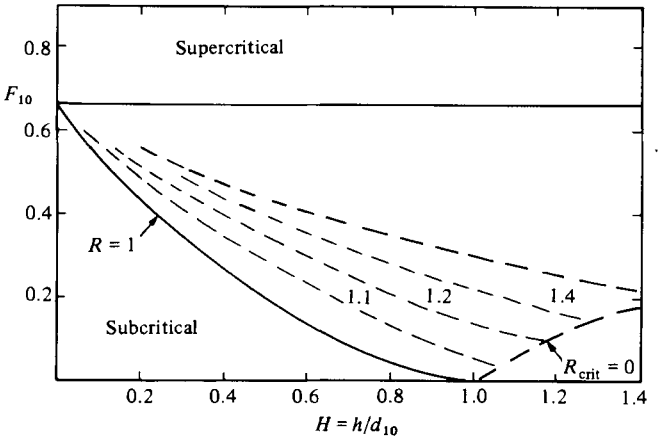

FIGURE 19. Same as figure 17 but for $r = 0.5$.

height. These curves remain horizontal in the rarefaction regions for larger H, for $r = 0.1$, 0.2, 0.35. The observed flow types in these figures compare very well with the theoretical regions, although the region where multiple states are predicted ($A'D'E'$ in figure 8) is to some extent an exception, and this is discussed below.

With regard to the agreement between the theoretical Γ, R curves and the observed values, the dependence of bore speed $F_{10}+\Gamma$ on R has been shown in figure 12. An inspection of these data points reveals no systematic dependence on H, so that Γ depends only on F_{10} and R. As discussed in §4, the agreement between theory and experiment is reasonable except where the bores become turbulent, in which case interfacial drag (neglected in the present theory) appears to result in a significant reduction of the bore speeds. The dependence of R on F_{10} and H is shown in figure 20 for $r = 0.035$, 0.1 and 0.2. Here the agreement is generally good, although there is a systematic tendency for the observed R-value to be larger than the theoretical one; this is consistent with the difference found in the results of figure 12. Long (1974) found quite good agreement between theory and experiment for the dependence of R on F_{10} and H for the case $r = 0.2$, $s = 1.0$.

In the regions where upstream rarefaction takes place, quantitative measurement of its magnitude was not possible because, in most cases, the length of the tank was insufficient for the flow to reach a steady state near the obstacle. The observations were, however, qualitatively consistent with theoretical expectations.

To compare the present results with those of Houghton & Isaacson (1970, hereinafter denoted by H & I), we refer to figure 20 ($r = 0.5$), which is equivalent to figures 5 and 11 of H & I. The rarefaction B of H & I is reproduced in figure 20, but, instead of the region B where H & I conclude that the flow is persistently unsteady, a hydraulic-drop region is found in the present experiments. No hydraulic drops were reported by H & I: this is possibly because flow separation in the lee of the obstacle is important to this phenomenon, and this is not represented by a two-layer numerical model. The nature of the observed hydraulic drops is discussed in more detail in the next section. Most of H & I's other results, involving substantial displacement of the free surface, are outside the range of the present study.

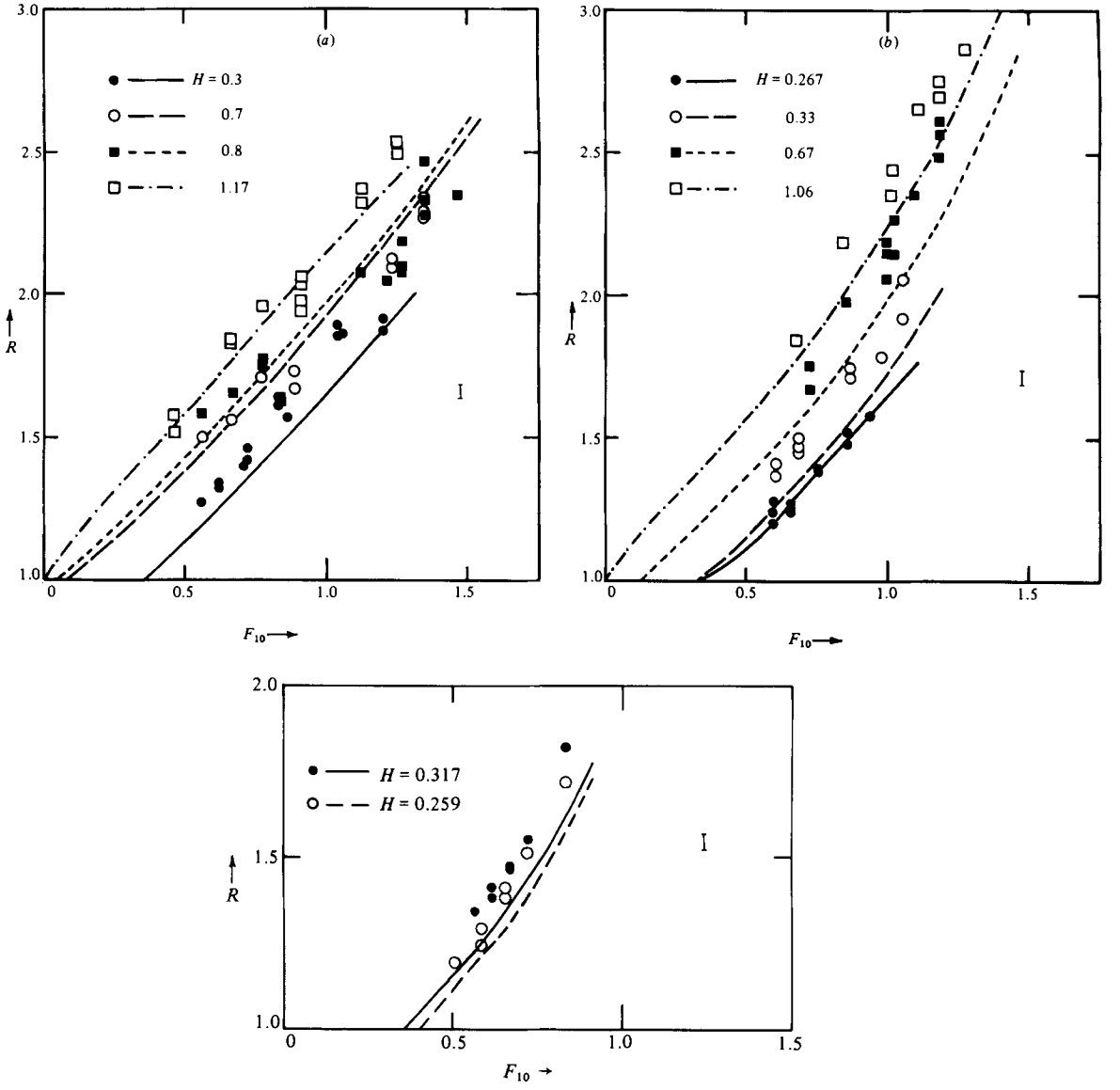

FIGURE 20. The dependence of upstream jump height R on F_{10} and H – comparison between theory and experiment. (*a*) $r = 0.035$; (*b*) 0.1; (*c*) 0.2.

Upstream multiple states

A series of runs was carried out to test the theoretical prediction of multiple states in the region $D'A'E'$ of figure 8, for $r = 0.035$. The results presented in figure 16 show that both supercritical and partially blocked (upstream bore) states were in fact obtained in part of this region, shown shaded in figure 21. Throughout region $D'A'E'$, the normal rapid start to a constant towing speed for the obstacle always resulted in supercritical flow. In order to realize partially blocked flow, it was necessary to commence towing at a speed such that F_{10} was below $A'E'$, and, after steady-state flow was reached near the obstacle, to increase the towing speed to values above $A'E'$. In these runs, it was evident that it was necessary to build up the upstream bore to

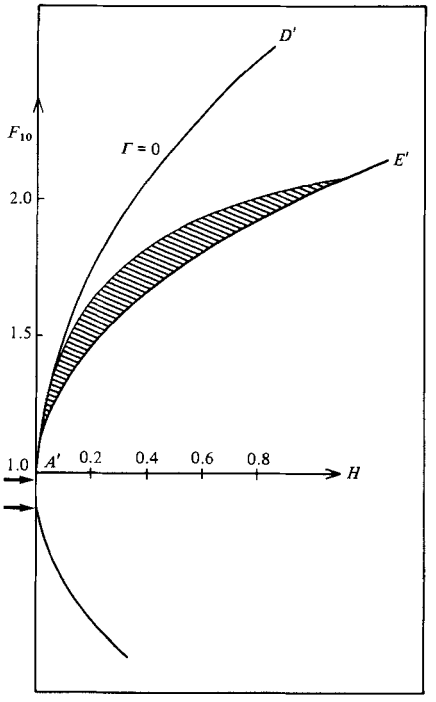

FIGURE 21. The region of the (F_{10}, H)-diagram where hysteresis in the upstream flow was observed, for $r = 0.035$.

a sufficiently large amplitude to enable it to move ahead of the obstacle when the speed was increased to values above $A'E'$.

In all cases where this phenomenon was observed, the relative upstream bore speed was very small. To demonstrate that the upstream bore actually moved further ahead after the maximum speed was attained in some cases, observations of the bore displacement relative to the obstacle are shown in figure 22 from three runs where the speed was increased from values below $A'E'$ to values above $A'E'$. In these runs, only one upstream bulge had time to develop, as shown in figure 23(*a*). After the increase in speed the bore (or bulge) at first remained in an approximately steady position relative to the obstacle whilst its height slowly increased, and it subsequently moved further ahead relative to the obstacle at a constant speed (figure 23*b*). Figure 23(*c*) shows the corresponding supercritical flow state, which in this case is realized for a lower towing speed ($F_{10} = 1.65$) than that for figures 23(*a*, *b*).

Despite numerous attempts, no steady-state upstream bores could be obtained in the region $D'A'E'$ other than the shaded region of figure 21. This can be attributed to the fact that observed speeds are slightly slower than the theoretical ones, particularly when the flow becomes turbulent for $R > 2.3$. Also, for states that were very close to the upper boundary of the shaded region, in some cases the upstream bore was stationary relative to the obstacle; in these cases the bore was conspicuously turbulent, and this interfacial drag is apparently responsible for the reduction in the relative bore speed.

For $r = 0.1$ the same procedure was utilized to search for multiple states in region $D'A'E'$, but only supercritical flow could be realized. The theoretical two-state region is much smaller here than for $r = 0.035$, and this failure to obtain blocked states is

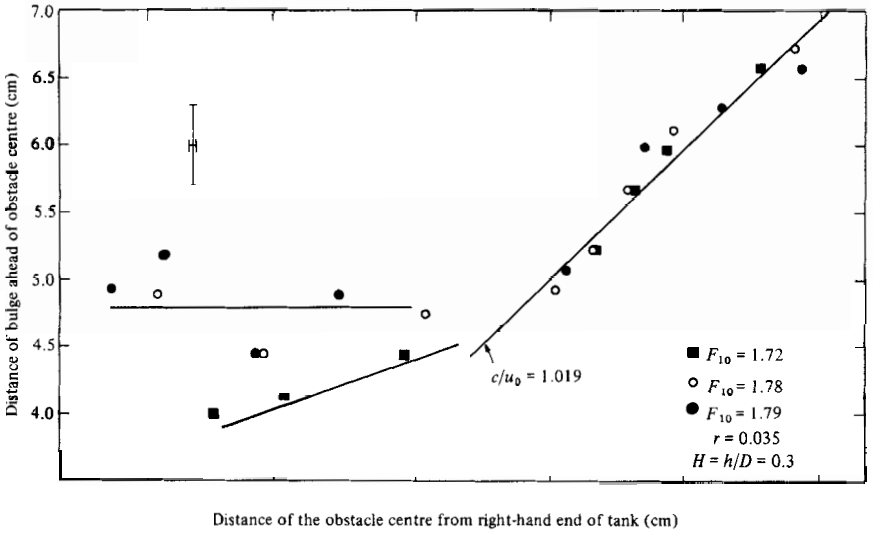

FIGURE 22. Evidence for two-state flows. Distance between the centre of the upstream bulge and the obstacle centre, as a function of distance along the tank, for three runs where the towing speed was initially substantially smaller, and then increased to a constant value, after which these observations were taken. Points with $400 < x < 550$ cm were recorded by camera C1, $550 < x < 700$ cm by camera C2.

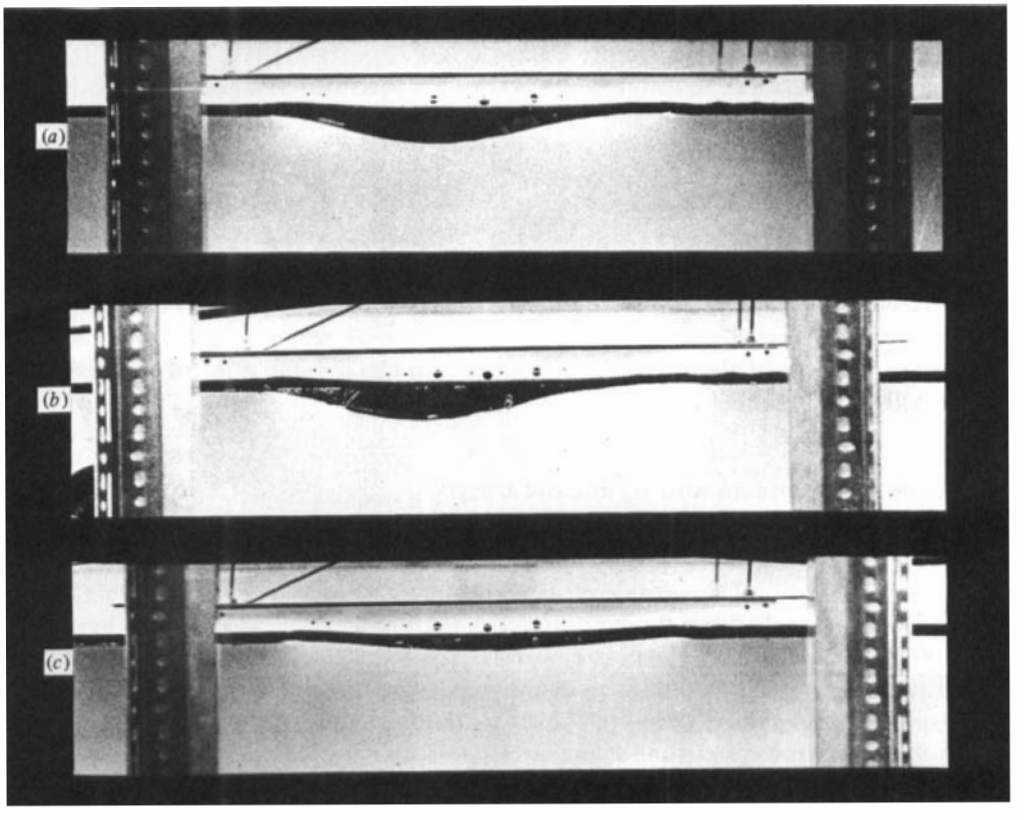

FIGURE 23. Observations from the run with $F_{10} = 1.79$ of figure 22. (*a*) $x = 489$ cm, where x is the abscissa of figure 22; (*b*) $x = 664$ cm; (*c*) supercritical flow for $F_{10} = 1.65$.

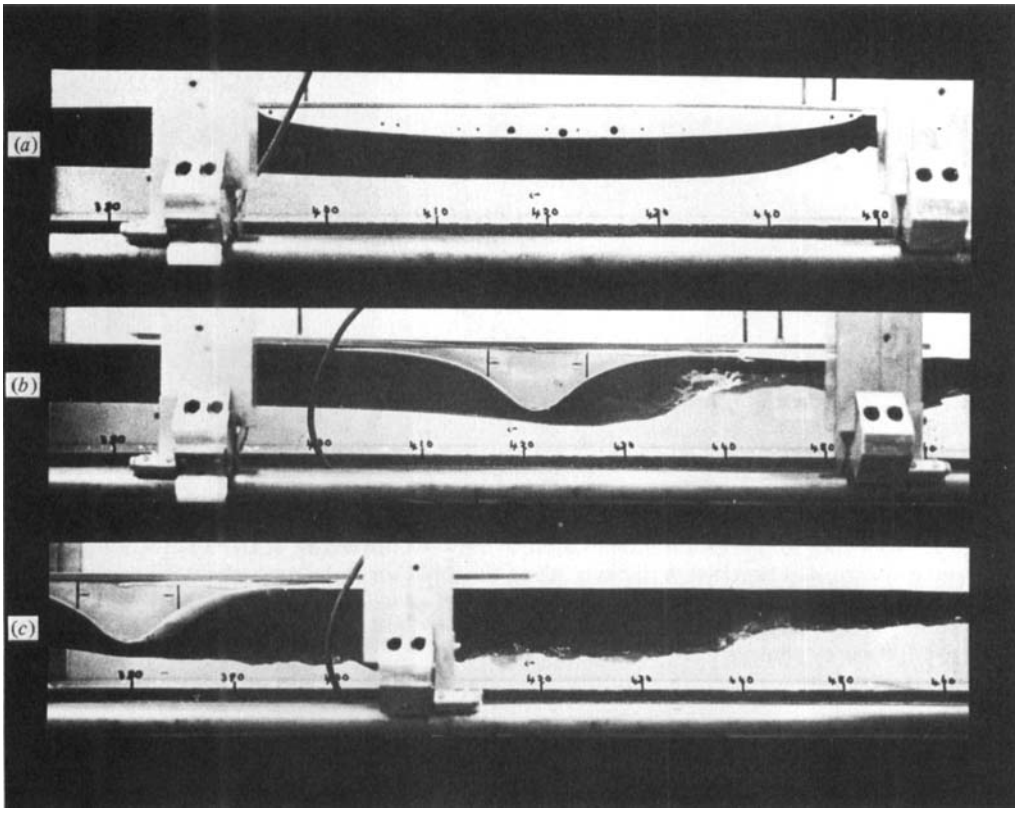

FIGURE 24. (*a*) A downstream undular hydraulic drop, $r = 0.35$, $F_{10} = 0.674$, $H = 0.686$. (*b*) Downstream turbulent hydraulic drop, $r = 0.35$, $F_{10} = 0.607$, $H = 1.6$. (*c*) As for (*b*), but with $F_{10} = 0.70$.

again attributed to the effect of interfacial drag on bore speeds. An inspection of the figures 17–19 shows that a small change in Γ results in a substantial displacement of the curve (Γ = constant) for $r = 0.1$, 0.2 and 0.35, particularly when Γ is small. The assumed effects of interfacial friction are largest when R is large, and this prevents the details of the theoretical diagrams in the regions $D'E'$ of figure 8 from being realized experimentally.

6. Downstream effects and hydraulic drops

In the preceding sections we have discussed the character of the flow upstream of the obstacle. In this section we give a relatively brief description of the nature of the observed flow over and downstream of the obstacle. Flow types A, B, C and D of figure 4 occur in single-layer flows and require no further discussion here. Flow types E and F are new, and their form is described below.

As stated in §3, as F_{10} and H are increased, the amplitude of the upstream interface displacement increases until the flow just upstream becomes almost (locally) critical. This is its maximum amplitude (since a larger-amplitude disturbance would travel more slowly than the obstacle speed), and for this case and other cases with larger F_{10} and/or H the flow over the obstacle is supercritical. The flow must still adjust to the downstream conditions, however, and since the upper layer is thicker upstream

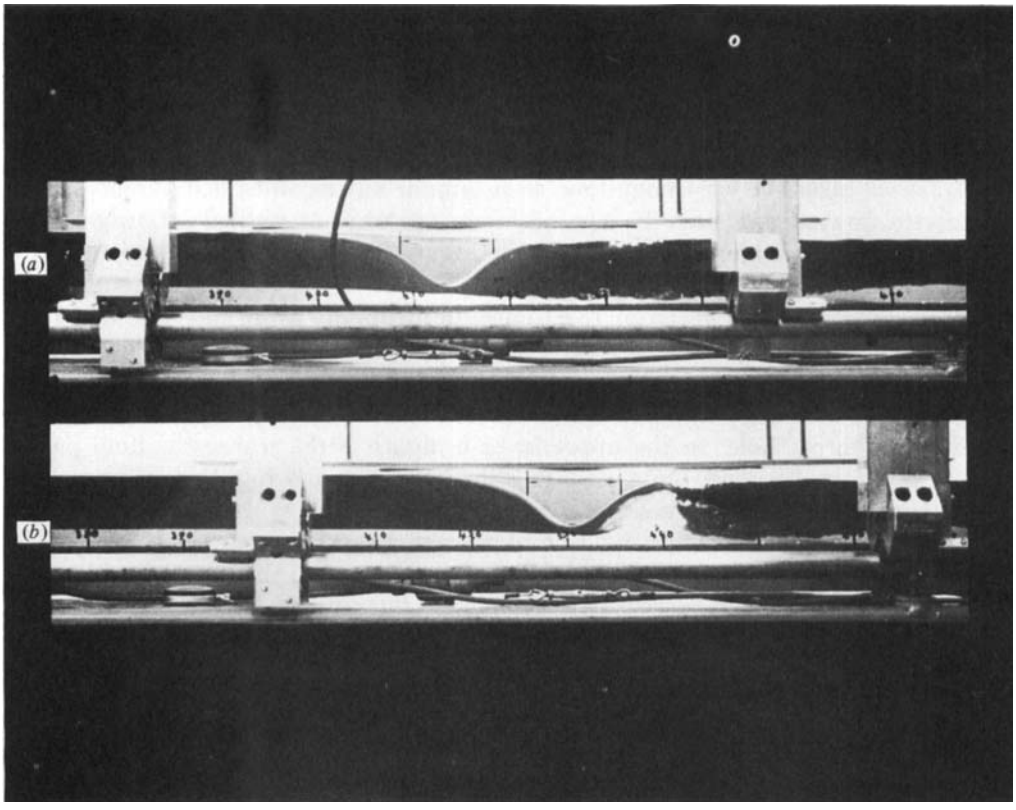

FIGURE 25. Example of two flow states for the same steady conditions, $r = 0.71$, $H = 1.04$. (*a*) $F_{10} = 0.357$, with towing speed reduced to this constant value. (*b*) $F_{10} = 0.358$, with towing speed increased to this constant value.

it must (by conservation of mass) be thinner downstream before, eventually, attaining its initial undisturbed state *far* downstream by means of a further hydraulic jump and/or rarefaction. For these situations the flows were observed to make this transition from one supercritical state to a conjugate supercritical one via an energy dissipating hydraulic drop. These drops may be laminar as shown in figure 24(*a*), or turbulent as in figures 24(*b*, *c*). Such drops were only obtained for $r = 0.35$ and $r = 0.5$ in these experiments, and in many cases a short obstacle was used, so that the hydrostatic assumption was not strictly valid. Nevertheless the observations were all found to be consistent with the necessary criteria for the above interpretation.

Equations for these flows are complicated by the fact that the flow is asymmetric over the obstacle, so that the form drag of the obstacle is probably significant. This means that conditions upstream and downstream of the obstacle cannot be easily related. The upstream and downstream flow states of the drops are approximately symmetrical, and energy loss occurs in the drop. Flow separation may be a significant factor in some drops, particularly for short obstacles.

Hydraulic drops were found in the regions $P'E'G'$ and $P'A'G'$ of figures 8(*d*) and 8(*e*) respectively, as expected, with flow type E. For sufficiently large H ($\gtrsim 0.4$) they were also found in the supercritical region above $A'G'$, where flow type 2F was obtained, but these were with the short steep obstacle M2. In the latter case it seems probable that separation was an essential ingredient in determining the flow

character. Figure 9 of Long (1954), reproduced in Baines & Davies (1980), is probably the first published example of flow type 2F.

Hydraulic drops and multiple states?

Some experimental runs with a relatively deep upper layer ($r = 0.71$) produced evidence that, under some circumstances, more than one steady state may exist here also. In these cases the upstream flows were similar but significant differences were found in the downstream flow. This parameter range was not studied extensively and we restrict description here to one example. Figure 25 shows two flows with nearly equal steady-state conditions. In figure 25 (*a*) ($F_{10} = 0.357$) the flow state was attained by establishing a towing speed of 15.51 cm/s immediately after start-up, and then subsequently decreasing it to 12.74 cm/s, after which the picture was taken; in figure 26 (*b*) the flow state was attained in a similar manner but instead the towing speed was *increased* from 9.89 cm/s to 12.79 cm/s. The main difference between the two flows is clearly the large 'hole' in the upper layer in figure 26 (*b*), where the fluid passes through a hydraulic drop–jump pair in which the jump is highly turbulent; the subsequent downstream flow is similar to that of figure 25 (*a*). Both of these flow states were stable and persisted over a distance of at least several metres. The towing speed was in the 'rarefaction' regime for the internal mode, and in the 'partially blocked' regime for the external mode, so that there is a difference in elevation of the free surface between upstream and downstream.

7. Discussion and summary

We have investigated the general nature of nonlinear two-layer quasi-hydrostatic flow of immiscible fluids over a long obstacle, in situations where only the internal (interfacial) mode is significant, and the layer containing the obstacle is not initially deeper than the other layer. The results are generally applicable to the two-layer systems where the internal mode is dominant (with minor quantitative changes), and have been carried out as part of a programme to understand the general character of the motion upstream of obstacles in geophysical flows. When the layer through which the obstacle moves is thin ($r \ll 1$) the flow has similar character to the well-known single-layer flow shown in figure 1; when the layers are of comparable depth ($r \approx 0.5$), on the other hand, the flow character is similar to that shown in figure 2 (ignoring the higher-order modes). The nature of the transition between these cases as r increases is shown in figure 8, and in more detail in figures 15–19; these provide a reasonably complete description of the flow character over a wide range of r-values up to 0.5.

The upstream motion may consist of an undular or turbulent internal bore, or an internal rarefaction, or a non-undular laminar bore with a rarefaction. The reasons for this variety of behaviour may be interpreted in terms of the variation of linear wave speed with layer depth ratio r, as shown in figure 7. Depending on the value of r, linear-wave speeds immediately upstream of the obstacle may vary with upstream-disturbance amplitude in any one of the three forms shown in figure 26 (*a*). The upper curve corresponds to an upstream bore (type 3 of figure 4), since larger disturbances travel faster and cause the upstream displacements to steepen. The central curve corresponds to upstream motion which takes the form of linear non-dispersive waves moving at constant speed; this is approximately the case for the continuously stratified fluid of figure 2 and for $r = 0.5$, at small amplitudes. The bottom curve corresponds to a rarefaction (type 5 of figure 4); here, larger disturbances travel more slowly and cause the upstream motion to spread out (amplitude-dependent

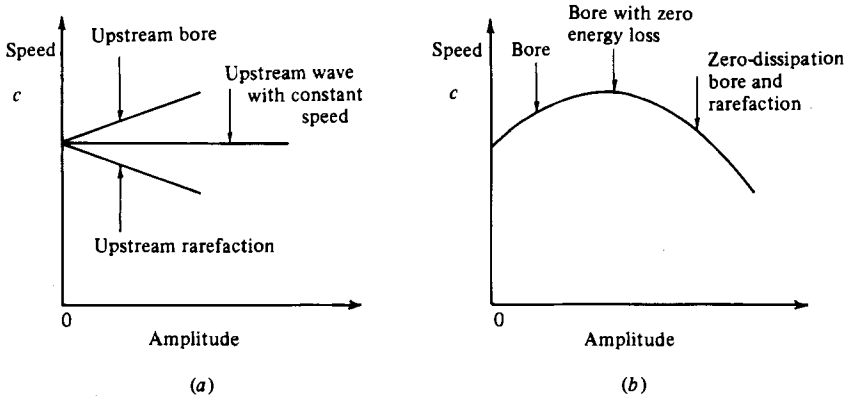

FIGURE 26. Representative diagrams of linear-wave speed immediately upstream of the obstacle as a function of the amplitude of the upstream disturbance.

dispersion). In some situations (e.g. figure 5(*d*), and other states in region $G'E'C'$ of figure 8(*d*)) the curve may take the form shown in figure 26(*b*), where the upstream motion consists of a bore at small amplitudes, but as this amplitude increases, the energy loss at the bore front decreases to zero so that the bore degenerates to a smooth transition of constant shape; a further increase in amplitude is then manifested as a rarefaction, which may be increased until the flow becomes locally critical. Beyond this point (i.e. this obstacle speed u_0) no further increase in upstream amplitude is possible.

We may note that of the two factors that one may expect to affect the propagation of upstream disturbances, namely nonlinear steepening and linear dispersion, the latter has virtually no effect on the upstream speed and amplitude, which are governed by nonlinear factors. Dispersion is, however, important in determining the *character* of the upstream motion; as with solitary waves, the nature of upstream undular bores is governed by a balance between these two factors, as discussed in §4, and interfacial friction is also significant for a steady state.

For hydrostatic flow, the interface at the obstacle crest must either have zero slope or be critical, as for single-layer flow. In two-layer flow this requirement can result in a downstream hydraulic drop, which may be laminar or turbulent. Whereas in hydraulic jumps the flow changes from supercritical to subcritical (moving downstream), in these hydraulic drops the flow changes from one supercritical state to another, with an associated energy loss.

Two separate examples of multiple states or 'hysteresis' in the flow were observed. First, the anticipated double state of figure 1 was confirmed for part of the expected region for $r = 0.035$, but could not be realized for higher values of r, because the observed bore speeds were less than the predicted theoretical ones. It is suspected that this discrepancy is due to interfacial stress, because the observations and theory appear to diverge more sharply once the observed bores become turbulent (figures 12*a*, *b*). Secondly, a new example, not fully understood, was observed downstream for large obstacles when $r = 0.71$, where the flow may or may not have a hydraulic drop and jump pair.

The present experiments were carried out with two immiscible fluids with a reasonably large density difference (density ratio $s = 0.79$). For comparison some qualitative runs were carried out with two miscible fluids (salty and fresh water) with a much smaller density difference ($s = 0.97$). Although quantitative comparisons were

not made, the observed flows were generally consistent with the immiscible results and the analysis of §3, except that turbulence and mixing in the upstream bores occurred much more readily than for the immiscible experiments. Consequently, for these theories to be applicable to geophysical situations some account must be taken of this behaviour, as the upstream bores may behave more like gravity currents than the large-amplitude undular structures described here, particularly at large amplitude.

Finally, we may note the relevance of these flows for flow in the atmosphere. Apart from the general contribution to knowledge of finite-amplitude effects of obstacles and mountain ranges, the results may be qualitatively applicable (with the modifications of the previous paragraph in mind) to certain situations where a low-level stable layer exists, surmounted by a weakly stratified layer. Reports of upstream motions of the type described here in the atmosphere are rare. This is probably because these upstream motions are most strongly manifested in the horizontal velocity, and hence they are not easily observed unless the winds are measured and, probably, their presence is anticipated. Most mountains are not two-dimensional, and the extent of these motions upstream will depend on the obstacle shape. One example has been reported by Edinger (1966) who described upstream waves (undular bore?) in a shallow stable layer off Point Sal, California, and gave a brief survey of some other similar observations. Whether or not such features as hydraulic drops are important for flows downstream of mountain ranges remains to be determined.

The author is most grateful to David Murray for his assistance at all stages of the experiments, and to Robert Bell for programming the rarefaction equations of §3. He is also grateful to two referees for a number of helpful comments which improved the manuscript, and to Roger Grimshaw for some enlightening discussions.

Appendix. The effect of viscous boundary layers on undular bore structure

We here estimate the magnitude of viscous boundary-layer effects on the function L (4.8). We consider an idealized model of the bore, where, for the purposes of this calculation, the bore front is regarded as a jump, the waves are ignored and a viscous boundary layer on each side of the interface is assumed. Viscous boundary layers will also be present on the tank floor and sidewalls. Axes are taken moving with the bore, and the origin is taken at the interface at the bore front. The velocities in the upper and lower layers are denoted respectively by

$$u_1 = U_1 + v_1, \quad u_2 = U_2 + v_2, \tag{A 1}$$

where U_1 and U_2 are the inviscid velocities and v_1 and v_2 the velocities resulting from stress at the interface. Changes in L are supposed to result from viscous processes only, and from (4.3) and (4.8) we have

$$L(x) \approx \rho_2 \int_{-d_{21}}^{0} (U_2^2 - (U_2+v_2)^2)\,\mathrm{d}z + \rho_1 \int_{0}^{d_{11}} (U_1^2 - (U_1+v_1)^2)\,\mathrm{d}z. \tag{A 2}$$

We first consider the contributions to L from the boundary layers at the interface, and denote these by L_i; corresponding contributions from the bottom and sidewall boundary layers are denoted by L_b, so that

$$L = L_\mathrm{i} + L_\mathrm{b}. \tag{A 3}$$

Assuming a steady state, making the customary boundary-layer assumptions and linearizing the equations for v_1 and v_2 results in a pair of diffusion equations (with x time-like) for v_1 and v_2, with the boundary conditions of continuity of velocity and equality of stress at the interface. The solution is mathematically complex and will not be pursued here, but substitution into (A 2) shows that

$$L_i(x) \approx -\rho_2 \int_{-d_{21}}^{0} v_2^2 \, dz - \rho_1 \int_{0}^{d_{11}} v_1^2 \, dz. \tag{A 4}$$

The upper and lower boundary layers have the lengthscales $2(\nu_1 x/U_1)^{\frac{1}{2}}$, $2(\nu_2 x/U_2)^{\frac{1}{2}}$ respectively, where ν_1 and ν_2 denote the viscosities of the respective fluids, and in order to estimate L_i we may take

$$\left.\begin{aligned} v_2 &= 0 \quad \left(-d_{21} < z < -2\left(\frac{\nu_2 x}{U_2}\right)^{\frac{1}{2}}\right), \\ &= -\tfrac{1}{2}(U_2 - U_1) \quad \left(-2\left(\frac{\nu_2 x}{U_2}\right)^{\frac{1}{2}} < z < 0\right), \\ v_1 &= \tfrac{1}{2}(U_2 - U_1) \quad \left(0 < z < 2\left(\frac{\nu_1 x}{U_1}\right)^{\frac{1}{2}}\right), \\ &= 0 \quad \left(2\left(\frac{\nu_1 x}{U_1}\right)^{\frac{1}{2}} < z < d_{11}\right). \end{aligned}\right\} \tag{A 5}$$

Substitution into (A 4) gives

$$L_i \approx -\tfrac{1}{2}(U_2 - U_1)^2 \left[\rho_1 \left(\frac{\nu_1}{U_1}\right)^{\frac{1}{2}} + \rho_2 \left(\frac{\nu_2}{U_2}\right)^{\frac{1}{2}}\right] x^{\frac{1}{2}}. \tag{A 6}$$

Applying the same procedure to the side and bottom boundary layers yields

$$\begin{aligned} L_b \approx -\rho_2 \left(1 + \frac{2d_{21}}{w}\right) (2U_2 + \tfrac{1}{2}(U_2 - c_1)) \, (\nu_2 x (U_2 - c_1))^{\frac{1}{2}} \\ + \rho_1 \frac{2d_{11}}{w} (2U_1 - \tfrac{1}{2}(c_1 - U_1)) \, (\nu_1 x (c_1 - U_1))^{\frac{1}{2}}, \end{aligned} \tag{A 7}$$

where c_1 is the bore speed and w is the tank width.

From conservation of mass we have

$$U_1 - c_1 = -U_1(R-1), \quad U_2 - c_1 = \frac{r}{1-r} U_2 (R-1), \quad U_2 - U_1 \simeq \frac{c_0(R-1)}{R(1-rR)}. \tag{A 8}$$

Taking $U_1 \sim U_2 \sim c_0$, $\nu_1 \sim \nu_2$, $\rho_1 \sim \rho_2$ we obtain

$$\begin{aligned} L \simeq -\rho_1 c_0^2 \left(\frac{\nu_1 x}{c_0}\right)^{\frac{1}{2}} \left[\frac{(R-1)^2}{R^2(1-rR)^2} + 2\left(\frac{r(R-1)}{1-r}\right)^{\frac{1}{2}} \left(1 + 2\frac{d_{21}}{w}\right) (1 + O(r(R-1)) \right. \\ \left. - 4\frac{d_{11}}{w} (R-1)^{\frac{1}{2}} (1 + O(R-1))\right] \end{aligned} \tag{A 9}$$

$$= -\rho_1 c_0^2 \left(\frac{\nu_1 x}{c_0}\right)^{\frac{1}{2}} g(R, r). \tag{A 10}$$

Additional effects due to the presence of waves will not affect this estimate greatly.

REFERENCES

ABLOWITZ, M. J., FOKAS, A. S., SATSUMA, J. & SEGUR, H. 1982 On the periodic intermediate long wave equation. *J. Phys.* A: *Math. & Gen.* **15**, 781–786.

BAINES, P. G. 1977 Upstream influence and Long's model in stratified flows. *J. Fluid Mech.* **82**, 147–159.

BAINES, P. G. 1979*a* Observations of stratified flow over two-dimensional obstacles in fluid of finite depth. *Tellus* **31**, 351–371.

BAINES, P. G. 1979*b* Observations of stratified flow past three-dimensional barriers. *J. Geophys. Res.* **83**, 7834–7838.

BAINES, P. G. & DAVIES, P. A. 1980 Laboratory studies of topographic effects in rotating and/or stratified fluids. In *Orographic Effects in Planetary Flows*, chap. 8, pp. 233–299. GARP Publication no. 23, WMO/ICSU.

BAINES, P. G. & GRIMSHAW, R. H. J. 1979 Stratified flow over finite obstacles with weak stratification. *Geophys. Astrophys. Fluid Dyn.* **13**, 317–334.

BENJAMIN, T. B. 1966 Internal waves of finite amplitude and permanent form. *J. Fluid Mech.* **25**, 241–270.

BENJAMIN, T. B. 1967 Internal waves of permanent form in fluids of great depth. *J. Fluid Mech.* **29**, 559–592.

BENJAMIN, T. B. & LIGHTHILL, M. J. 1954 On cnoidal waves and bores. *Proc. R. Soc. Lond.* A **224**, 448–460.

BYATT-SMITH, J. G. B. 1971 The effect of laminar viscosity on the solution of the undular bore. *J. Fluid Mech.* **48**, 33–40.

CHU, V. H. & BADDOUR, R. E. 1977 Surges, waves and mixing in two-layer density stratified flow. In *Proc. 17th Congr. Intl Assoc. Hydraul. Res.*, vol. 1, pp. 303–310.

EDINGER, J. G. 1966 Wave clouds in the marine layer upwind of Pt. Sal, California. *J. Appl. Met.* **5**, 804–809.

FORNBERG, B. & WHITHAM, G. B. 1978 A numerical and theoretical study of certain non-linear wave phenomena. *Phil. Trans. R. Soc. Lond.* A **289**, 373–404.

HOUGHTON, D. D. & ISAACSON, E. 1970 Mountain winds. *Stud. Numer. Anal.* **2**, 21–52.

HOUGHTON, D. D. & KASAHARA, A. 1968 Nonlinear shallow fluid over an isolated ridge. *Commun. Pure Appl. Maths* **21**, 1–23.

JOSEPH, R. I. 1977 Solitary waves in a finite depth fluid. *J. Phys.* A: *Math. & Gen.* **19**, L225–L227.

KEADY, G. 1971 Upstream influence on a two-fluid system. *J. Fluid Mech.* **49**, 373–384.

KOOP, C. G. & BUTLER, G. 1981 An investigation of internal solitary waves in a two-fluid system. *J. Fluid Mech.* **112**, 225–251.

KUBOTA, T., KO, D. R. S. & DOBBS, L. 1978 Weakly-nonlinear, long internal gravity waves in stratified fluids of finite depth. *AIAA J. Hydronautics* **12**, 157–165.

LONG, R. R. 1954 Some aspects of the flow of stratified fluids, II. Experiments with a two-fluid system. *Tellus* **6**, 97–115.

LONG, R. R. 1955 Some aspects of the flow of stratified fluids, III. Continuous density gradients. *Tellus* **7**, 341–357.

LONG, R. R. 1970 Blocking effects in flow over obstacles. *Tellus* **22**, 471–480.

LONG, R. R. 1974 Some experimental observations of upstream disturbances in a two-fluid system. *Tellus* **26**, 313–317.

MCINTYRE, M. E. 1972 On Long's hypothesis of no upstream influence in uniformly stratified or rotating flow. *J. Fluid Mech.* **52**, 209–243.

MILES, J. W. 1968 Lee waves in a stratified flow. Part 2. Semi-circular obstacle. *J. Fluid Mech.* **33**, 803–814.

ONO, H. 1975 Algebraic solitary waves in stratified fluids. *J. Phys. Soc. Japan* **39**, 1082–1091.

PEREGRINE, D. H. 1966 Calculations of the development of an undular bore. *J. Fluid Mech.* **25**, 321–330.

PRATT, L. J. 1983 A note on nonlinear flow over obstacles. *Geophys. Astrophys. Fluid Dyn.* **24**, 63–68.

SEGUR, H. & HAMMACK, J. L. 1982 Soliton models of long internal waves. *J. Fluid Mech.* **118**, 285–304.

SMITH, R. B. 1976 The generation of lee waves by the Blue Ridge. *J. Atmos. Sci.* **33**, 507–519.

STOKER, J. J. 1953 Unsteady waves on a running stream. *Comm. Pure Appl. Math.* **6**, 471–481.

STURTEVANT, B. 1965 Implications of experiments on the weak undular bore. *Phys. Fluids* **8**, 1052–1055.

SU, C. H. 1976 Hydraulic jumps in an incompressible stratified fluid. *J. Fluid Mech.* **73**, 33–47.

WOOD, I. R. & SIMPSON J. E. 1984 Jumps in layered miscible fluids. *J. Fluid Mech.* **140**, 329–342.

YIH, C.-S. & GUHA, C. R. 1955 Hydraulic jump in a fluid system of two layers. *Tellus* **7**, 358–366.